Numerical Study of Explosively Developing Extratropical Cyclones in the Northwestern Pacific Region

Akira Kuwano-Yoshida* and Yoshio Asuma**

Division of Earth and Planetary Sciences, Graduate School of Science,

Hokkaido University, Sapporo, Japan

*current affiliation

Earth Simulator Center, Japan Agency for Marine-Earth

Science and Technology, Yokohama, Japan

**current affiliation

Department of Physics and Earth Sciences, Faculty of Science,

University of the Ryukyus, Okinawa, Japan

Submitted to Monthly Weather Review as an article on 1 December 2006

Revised on 16 April 2007

Corresponding author

Akira Kuwano-Yoshida

Earth Simulator Center, Japan Agency for Marine-Earth Science and Technology, Japan

3173-25, Showa-machi, Kanazawa-ku, Yokohama City, Kanagawa, 236-0001

e-mail: akiray@jamstec.go.jp

phone: +81-45-778-5866, fax: +81-45-778-5492

Abstract

Numerical simulations of six explosively developing extratropical cyclones in the northwestern Pacific region are conducted using a regional meso-scale numerical model (PSU-NCAR MM5). Cyclones are categorized according to the locations where they form and develop: Okhotsk-Japan Sea (OJ) cyclones originate over the eastern Asian continent and develop over the Sea of Japan or the Sea of Okhotsk; Pacific Ocean-Land (PO-L) cyclones also form over the Asian continent and develop over the northwestern Pacific Ocean; Pacific Ocean-Ocean (PO-O) cyclones form and develop over the northwestern Pacific Ocean. Two cases (the most extreme and normal deepening rate cases for each cyclone type) are selected and simulated. Simulations show that the extreme cyclone of each type is characterized by a different meso-scale structure and evolutionary path, which strongly reflect the larger scale environment: OJ cyclone has the smallest deepening rates, associated with a distinct upper-level shortwave trough, a clear lower-level cold front, and a precipitation area that is far from the cyclone center; PO-L cyclone has moderate deepening rates with high propagation speeds under zonally stretched upper-level jets; PO-O cyclone has the strongest deepening rates associated with large amounts of precipitation near its center. Sensitivity experiments to the latent heat release associated with water vapor condensation show that PO-O cyclones rarely develop without a release of latent heat and their structures are drastically different from the control runs, while OJ cyclones exhibit almost the same developments and have similar structures to the control runs. These tendencies can be seen both extreme and normal

deepening rate cases. These results reveal that the importance of latent heat release to explosive cyclone development varies among the cyclone types, reflected by the cyclone origin, frontal structure, moisture distribution and jet stream configuration.

1. Introduction

Initial study of explosively developing cyclones by Sanders and Gyakum (1980) was followed by many numerical studies conducted to enhance knowledge of the systems that cause the strong winds, heavy precipitation and floods accompanying cyclones. However, forecasting of such cyclones has been difficult (Harr et al. 1992; Sanders et al. 2000) due to a poor understanding of the cyclone processes, including the upper-level short-wave trough, lower-level baroclinity, and their interactions in the presence of diabatic heating (Shapiro et al 1999; Kuo et al. 1991). Scientific interest has also focused on the energy and vapor transport of explosive cyclones, providing the mechanisms for their rapid development and their contribution to local and global climate changes.

Statistical analyses (Sanders and Gyakum 1980; Roebber 1984) have shown that the northwestern Pacific region is one of the most active areas for explosive cyclone development. Chen et al. (1992) and Yoshida and Asuma (2004) identified two active areas in the northwestern Pacific region: one over the Sea of Japan and the Sea of Okhotsk; another over the northwestern Pacific Ocean. Several case studies and numerical studies for cyclone development in the northwestern Pacific region have been conducted (Liou and Elsberry 1987; Mullen and Baumhefner 1988; Takano 2002). Chen and Dell'Osso (1987) simulated cyclone development over the Sea of Japan and suggested the importance of latent heat release and the presence of a low-level jet for the cyclone development. Nuss and Kamikawa (1990) compared the explosive cyclone with the non-explosive cyclone that developed over the northwestern Pacific Ocean and reported that the maintenance of strong surface fluxes in the updraft region is attributed to the interaction of warm frontal dynamics with a down stream upper-level jet streak, leading to the explosive cyclogenesis. These studies suggested that explosive cyclogenesis requires not only baroclinity but also diabatic heating. Kuo and Low-Nam (1990) simulated nine explosive cyclones over the western Atlantic Ocean and concluded that the influence of diabatic heating on explosive development varied substantially for each case. However, their study did not provide discussion of reasons for the variation.

Yoshida and Asuma (2004) classified explosively developing extratropical cyclones over the northwestern Pacific region into three types, based on the locations of formation and most rapid deepening: Okhotsk-Japan Sea (OJ) cyclones form over the Asian continent and develop over the Sea of Japan or the Sea of Okhotsk; Pacific Ocean-Land (PO-L) cyclones also form over the Asian continent and develop over the northwestern Pacific Ocean; Pacific Ocean-Ocean (PO-O) cyclones form and develop over the northwestern Pacific Ocean.

The authors concluded that each type of cyclone reflects the characteristic environmental and meso-scale structures at the location of most rapid development and the contributing development factors systematically reflect the larger-scale atmospheric environment. OJ cyclones frequently occur in late autumn, have the smallest deepening rates, and upper-level vorticity advection with a short-wave trough and lower-level thermal advection are essential for their development. PO-L cyclones have moderate deepening rates, frequently occur in early and late winter, and develop under a zonally extended jet stream. PO-O cyclones mainly occur in midwinter, have the largest deepening rates and develop with a large amount of latent heat release near the cyclone center. The main objectives of the present paper are to investigate the development of extreme cases of each cyclone type and to clarify the role of latent heat release and other processes in the explosive cyclogenesis using numerical simulations and analyses.

2. Data and model description

The Pennsylvania State University-National Center for Atmospheric Research (PSU-NCAR) fifth-generation Mesoscale Model (MM5) version 3.6.1, which is a non-hydrostatic, primitive-equation model (Grell et al. 1995), was used in the present study. Simulations were started 24 hours before the maximum observed deepening rate and integrated for 48 hours. Two nested grid domains with two-way nesting were used with the

Lambert conformal projection map. The horizontal resolution of the outer domain was 45 km having 200 x 160 grid points and that of the inner domain was 15 km having 301 x 301 grid points. The center of the each domain was set to be the surface cyclone center at the location of the maximum deepening rate. 23 vertical layers, with sigma coordinates from the surface to 100 hPa, were calculated. The explicit simple ice moisture scheme, which predicts water vapor, cloud water, and rainwater composition for air temperatures above $0^{o}C$, and cloud ice and snow composition below $0^{o}C$, was used as the outer domain (Dudhia 1989). A mixed-phase explicit moisture scheme, which also predicted supercooled water along with the simple ice scheme, was used for the inner domain (Reisner et al. 1998). Grell's cumulus parameterization (Grell 1993) was used to represent subgrid-scale convective precipitation for each domain.

The global objectively analyzed dataset (GANAL), provided by the Japan Meteorological Agency (JMA), was used for initial and lateral boundary conditions. The GANAL dataset contains sea level pressures, geopotential heights, temperatures, horizontal winds, and dewpoint depressions with horizontal resolutions of 1.25 degrees in latitude and longitude and 18 vertical levels between the surface and 10 hPa. A Reynolds sea surface temperature (SST) dataset, provided by the National Oceanic and Atmospheric Administration-Cooperative Institute for Research in Environmental Sciences Climate Diagnostics Center (NOAA-CIRES CDC), was used as the SST condition. This dataset provides a weekly mean SST for every

1-degree grid point in latitude and longitude.

3. Methodology and Results

a. Selection of extreme cases

The "Eady index" (σ_{BI}), derived by Lindzen and Farrell (1980), indicates the maximum growth rate of an adiabatic perturbation in quasi-geostrophic baroclinic flow on a β plane with a constant vertical wind shear and static stability, is used to diagnose the mid-latitude cyclone growth rate, and is defined as follows:

$$\sigma_{BI} = 0.31 \frac{f}{N} \left| \frac{\partial \mathbf{v}}{\partial z} \right|, \tag{1}$$

where **v** is the horizontal wind, f is the Coriolis parameter, N is the Brunt-Väisällä frequency and z is the height. The explosive cyclone's deepening rates (Bergeron) have been evaluated based on the sea level pressures at the cyclone center following Sanders and Gyakum (1980). Yoshida and Asuma (2004) calculated the deepening rate using the following definition:

$$\text{Cyclone deepening rate} = \left\{ \frac{p(t-6) - p(t+6)}{12} \right\} \frac{\sin 60°}{\sin \dfrac{\phi(t-6) + \phi(t+6)}{2}}, \tag{2}$$

where t is analyzed time in hours, p is the sea level pressure at the cyclone center, and ϕ is the latitude at the cyclone center. An explosively developing cyclone was defined as having a deepening rate of at least 1 Bergeron. Although the definition of Bergeron in Sanders and Gyakum (1980) used a 24-hour pressure change, a 12-hour pressure change is used by Yoshida and Asuma (2004) and in the present paper to find the instance of most rapid deepening in a cyclone's life.

To compare the growth rates of actual cyclones with those determined using the adiabatic linear baroclinic theory, the Eady index was calculated at the maximum deepening rate for all extratropical cyclones that continued for at least 2 days during three cold seasons from 1 October 1996 to 31 March 1999. Figure 1 shows a scatter diagram correlating the maximum deepening rates and the Eady indices at 650 hPa, which were calculated for 300 and 1000 hPa winds and potential temperatures 6 hours before the occurrence of the maximum deepening rate, and the values were averaged over the 1000 km area surrounding the cyclone center.

The slope of the regression line measures the extent to which the adiabatic (dry) baroclinic theory explains the cyclone-deepening rate. Although each panel shows a positive correlation between the maximum deepening rates and the Eady indices, above a 99% significance level, OJ cyclones show the smallest regression line slope (about 1.2 Bergeron $(day^{-1})^{-1}$), among the three types, while PO-L and PO-O cyclones have larger slopes (about 1.6 and 1.7 Bergeron $(day^{-1})^{-1}$, respectively). Several extreme cases, which had larger deepening rates, fall distinctly large distances from their regression lines. It is interesting that the Eady index does not exceed 1.5 day^{-1}, and the maximum deepening rate seems not to have maximum limitation, especially for the region in which the Eady index is larger than 1 day^{-1}. These results suggest that the explosive cyclogenesis cannot be explained simply on the basis of the Eady index by assuming adiabatic (dry) baroclinic instability, especially for larger deepening rates. To explain these results, the most rapidly developing cyclones in each of the three types, were selected and simulated using PSU-NCAR MM5.

b. Synoptic overview of extreme three cases

A synoptic overview of the extreme cases was developed using the GANAL dataset. Figure 2 shows the cyclone track and a time series of the central sea-level pressures for each extreme case from formation to disappearance. Figures 3, 4 and 5 show the distributions of sea level pressures, potential temperatures and their horizontal gradients at 850 hPa; geopotential heights, potential vorticities, and wind speeds at 300 hPa; at the time of maximum deepening rate, as well as 24 hours before and after the occurrence of the maximum deepening rate for the extreme OJ case; PO-L; and, PO-O, respectively.

The extreme OJ cyclone formed over the Asian continent at 1800 UTC 24 February 1999 (Fig. 2a), moved eastward and arrived over the northern Sea of Japan, with a 1004 hPa central sea-level pressure recorded 24 hours before the maximum deepening rate (Figs. 3a and b). The cyclone’s cold front extended along the east coast of the Asian continent, bending westward at 40°N. Another weak frontal system existed over the southwestern part of the Japanese mainland (Honshu), the East China Sea and southern China. A strong anticyclone formed over Mongolia, with a central sea-level pressure of 1044 hPa, and extended over the Asian continent. A weak jet streak appeared at the leading edge of an upper-level trough extending from Siberia, accompanied by a large potential vorticity (PV), which existed over the east coast of the Asian continent at 300 hPa. When the cyclone moved over the Sea of Okhotsk at 1200 UTC 27 February 1999 (Figs. 3c and d), it experienced its maximum deepening rate of 1.84 Bergeron (Table 1) and its central sea-level pressure dropped to 972 hPa. The two frontal zones merged and became a strong cold frontal zone elongating from the cyclone center to the southwest over the northwestern Pacific Ocean. A PV maximum, associated with the upper-level trough, existed over the Sea of Japan, just to the west of the surface cyclone center. The cyclone then moved northeastward at 1200 UTC 28 February 1999 (Figs. 3e and f), and its central sea-level pressure dropped further to 960 hPa, which was the minimum recorded throughout the cyclone life. The cold front elongated southeastward from the cyclone center, bending southwestward over the northwestern Pacific Ocean. The upper PV maximum overlapped the surface cyclone and the enlarged upper-level trough meandered. After the deepening, the cyclone stagnated, achieving its minimum central sea-level pressure of 960 hPa at 0600 UTC 28 February 1999 and disappearing at 1200 UTC 3 March 1999.

The cyclone track and the central sea-level pressures for the extreme PO-L cyclone are shown in Figs. 2c and d. The cyclone formed over the Asian continent at 0600 UTC 8 February 1998, moved rapidly eastward and located over the southern coast of the Sea of Japan at 1800 UTC 9 February 1998 (Figs. 4a and b; 24 hours before the maximum deepening rate appeared) and its central sea-level pressure at formation was 1010 hPa. A weak frontal zone extended just north of the surface cyclone. We can also see that a large cyclone existed over the central North Pacific Ocean and a relatively weak anticyclone (1024 hPa) formed over China. At 300 hPa, a strong jet stream zonally extended from southern China to the northeastern Pacific Ocean and a northern jet stream associated with a weak upper-level trough entered the stronger jet east of the surface cyclone. The cyclone continued to rapidly move eastward, explosively developing, 2.54 Bergeron (Table 1), offshore east of Japan at 1800 UTC 10 February 1998 and its central sea-level pressure at the time of maximum deepening dropped to 992 hPa (Figs. 4c and d). There was no distinct frontal structure in the lower level and the upper-level jet stream maintained its strength. Its central sea-level pressure dropped to a first minimum at 971 hPa at 1800 UTC 11 February 1998 (Fig. 4e). After short filling, it redeveloped and reached the 962 hPa minimum pressure of the cyclone lifecycle at 1200 UTC 13 February 1998, disappearing over the Gulf of Alaska at 0000 UTC 16 February 1998.

The extreme PO-O cyclone formed off the east coast of China at 0000 UTC 29 December 1997. Moving northeastward, the cyclone located over the south coast of Japan at 0000 UTC 30 December 1997 with its central sea-level pressure at 1009 hPa (Fig. 2e, f, and 5a). The cyclone had a very weak baroclinic zone extending between the south of China and south coast of Japan. An upper-level jet stream core was located over the lower-level baroclinic zone and second strong wind existed along the northeast of the cyclone (Fig. 5b). The surface cyclone formed under the southern entrance of the northeastern jet streak and the northern exit of the southwestern one. This is favorable for cyclogenesis because the jet streaks forced ageostrophic upward winds at that location (Keyser and Shapiro, 1986). The cyclone experienced explosive development over the northwestern Pacific Ocean at 0000 UTC 31 December 1997, 2.96 Bergeron (Table 1). The cyclone developed to 974 hPa and its cold front elongated southward. 300 hPa jets intensified southwest and northeast of the surface cyclone. The cyclone continued moving northeastward and the central sea-level pressure minimized to 957 hPa by 0000 UTC 1 January 1998 (Fig. 5e). The southern upper-level jet streak remained along the southern coast of Japan, separating from the surface cyclone center, while the northern jet streak continued to exist near the cyclone (Fig. 5f). The cyclone then turned northwestward, filling rapidly, and disappearing north of the Sea of Okhotsk at 0600 UTC 2 January 1998.

c. Control experiments

Simulation results for the extreme OJ cyclone (OJ CNTL run) are shown in Fig. 6. Simulated maximum deepening rates and deepening rates at T = 24 h are listed in Table 1. A cyclone associated with an upper-level short-wave trough was simulated over the northern Sea of Japan at T = 12 h (0000 UTC 27 February 1999, Figs. 6a and b). An upper-level positive PV anomaly from the 2-day average was located at the southern edge of the trough and a relatively weak jet streak appeared over the southern Sea of Japan. The precipitable water, over 30 mm, existed along the southern coast of Japan and precipitation occurred in the humid region. The northern frontal zone, within which no amount of precipitation occurred, can be identified and is the same as the results of GANAL analysis in Fig. 3a. As the cyclone developed, the upper-level positive PV anomaly moved over the south of the surface cyclone center and the upper-level jet streak elongated northeastward (Figs. 6d and f). The negative PV anomaly enhanced the east of the jet streak. Vertically integrated rainwater increased along the southern cold front, but was not remarkable around the cyclone center (Figs. 6c and e). The cyclone deepening rate at T = 24 h (1200 UTC 27 February 1999) was 1.55 Bergeron, smaller than that determined through the GANAL analysis, 1.84 Bergeron. The maximum deepening rate of the control run was 1.70 Bergeron at T = 30 h (1800 UTC 27 February 1999). Although there was a 6-hour lag in appearance time, it was almost comparable in magnitude to that determined using the GANAL analysis.

The results for the PO-L CNTL run are shown in Fig. 7. At T = 12 h (0600UTC 10 February 1998, Figs. 7a and b), the surface cyclone center was located just east of Japan. In the upper level, a jet stream zonally extended along the southern coast of Japan and a small trough associated with a high PV anomaly existed over the west of the surface cyclone (Figs. 7b and d). As the upper-level trough moved over the surface cyclone center at T = 36 h (Fig. 7f), the surface cyclone developed and its central sea-level pressure minimized. Precipitation appeared near the cyclone center, with a narrow larger region of precipitable water extending southwestward from the cyclone center. The upper-level negative anomaly, located to the east of the surface cyclone, and short ridge developed in the same region. Although the GANAL analysis showed a cyclone deepening rate of 2.54 Bergeron, the control run showed 1.62 Bergeron at T = 24 h. The maximum deepening rate was recorded at T = 18 h, although the deepening rate, 2.01 Bergeron, was also smaller than that determined in the GANAL analysis (Table 1), while the cyclone position and surface central sea-level pressure variation were simulated well as shown in Figs. 2c and d.

Figure 8 shows the results for the PO-O CNTL run. At T = 12 h (1200UTC 30 December 1997, Figs. 8a and b), the surface cyclone was located over the eastern coast of Japan and the moist region spread around the cyclone center and eastward. The precipitation volume was the largest among the three cases, which is over 2 mm (Fig. 8c). In the upper level, a jet streak located at the southwest of the surface cyclone center and another weaker jet streak appeared at the northeast. At T = 24 h (0000 UTC 31 December 1997, Figs. 8c and d), the positive PV anomaly overlapped the surface cyclone center and the northeastern jet streak strengthened as well as the northeastern negative PV anomaly. A larger amount of precipitable water was concentrated just east of the surface cyclone center, and the precipitation amount was also larger. At T = 36 h (1200 UTC, Figs. 8e and f), the larger precipitation and moisture area separated from the cyclone center and weakened. At the same moment, the northeastern jet streak weakened and spread and the southwestern one maintained its strength. Both of the deepening rates, 2.26 Bergeron at T = 24 h and 2.64 Bergeron at T = 18 h, which was the maximum deepening rate, were comparable to those in the GANAL analysis of 2.96 Bergeron.

d. Sensitivity experiments

Yoshida and Asuma (2004) suggested that contribution of latent heat release to cyclone deepening depended on the cyclone type. Numerical simulations also suggested different features for the relative configuration of precipitation area and the surface cyclone center, and the precipitation amount. To clarify how latent heat release affects cyclone development, sensitivity experiments were conducted and are described in this section. The simulations were conducted in the same manner described in the previous section, except that no latent heat release occurred during the water vapor condensation. The cyclone tracks and central sea-level pressures of simulations with (CNTL) and without (DRY) the latent heat release are summarized in Fig. 2 (dashed line and dotted line, respectively, in each panel) and the deepening rates at T = 24 h and the maximum deepening rate of each simulation are listed in Table 1.

The results of the no-latent heat release simulation for the extreme OJ cyclone (hereafter, OJ DRY run) are shown in Figs. 9a and b. Compared with the OJ CNTL (Figs. 6a and b), the cyclone meso-scale structures are not very different from each other and the cyclone tracks were similar (Figs. 2a and b), although the deepening rate (0.88 Bergeron at T = 24 h) was weaker than the OJ CNTL. The amounts of vertically integrated rain water and precipitable water slightly decreased for the DRY run (Figs. 6c and 9c), and the northward extension of the upper-level jet streak was reduced at T = 24 h (Figs. 6d and 9d) and T = 36 h (Figs. 6f and 9f). The simultaneous weakness of upper-level negative PV anomaly and upper-level jet reveals that the latent heat release enhanced updraft around the cold front and strengthened divergence in the upper levels. The divergence created an upper-level negative PV anomaly, which induced anticyclonic circulation. As a result, the upper-level jet streak extended northward. The minimum central sea-level pressure of the DRY run was about 10 hPa higher than that of GANAL analysis and 17 hPa higher than that of CNTL run (Fig. 2d).

To examine the three-dimensional structural differences between CNTL and DRY runs, the trajectory analysis of air parcels was conducted. In total, 343 air parcels around the cyclone center were traced. The parcels initiated from 7 x 7 points (each point horizontally separated by 225 km (15 grid points), each centered at the cyclone surface center, extending vertically 7 levels: 200, 300, 400, 500, 600, 700, and 850 hPa), as shown in Fig. 12. Trajectories were obtained for 24 hours back and forward from T = 24 h. Winds were interpolated every 15 minutes using 2 hour interval model outputs. Figure 13 shows the perspective views of the trajectories categorized by their mean distances into 4 groups using Ward's clustering method (Ward 1963), which clusters to minimize the sum of squared distances to the central mean of each cluster. Green lines correspond to the trajectories moving almost horizontally in upper levels, purple lines are upward moving air parcels in the mid-level, orange lines are downward moving air parcels from the cyclone's upstream at 200 – 400 hPa to surface cyclone, and blue lines are upward moving air parcels from the lower level.

Comparing the OJ CNTL run (Fig. 13a) with the OJ DRY run (Fig. 13b), the number of downward moving air parcels in the DRY run is lower than in the CNTL run and the number of mid-level upward moving parcels in the DRY run is higher than in the CNTL run. These are reflected in the decreased altitude attained by the upward parcels. Figs. 14a and b show the vertical cross sections along line A-A' in Fig. 6c and B-B' in Fig. 9c, the projected upward moving air parcels from the lower levels (blue lines). The upper-level positive PV anomaly is located just upstream of the upward trajectories in the OJ CNTL run, however, the upper-level positive PV anomaly is weaker in the OJ DRY run. In the CNTL run, air parcels reached the cyclone center from the southward direction in the lower level, suddenly rising to a height of 7 km, which corresponds to the tropopause, and the isentropic gradient below 6 km was steeper at cyclone downstream than that of the DRY run. This indicates that a larger amount of warm advection was associated with cyclone development in the CNTL run. However, trajectories in the DRY run were different from those in the CNTL run. Air parcels in the DRY run rose gradually along the isentropic surfaces and were lifted only up to a height of 5 km, which are altitudes below the tropopause.

The deepening rate in the PO-L DRY run decreased 0.73 Bergeron from 1.62 Bergeron in the CNTL run at T = 24 h, as shown in Table 1. The results of the DRY run for the extreme PO-L cyclone are shown in Fig. 10. There are distinct differences from the CNTL run in the precipitation and moisture distributions (Fig. 7). Although most of the vertically integrated rainwater was concentrated along the cold frontal zone in the CNTL run, it was spread over the warm sector during the DRY run. The amount of precipitable water in the DRY run was less than that in the CNTL run due to a smaller lower-level convergence in the warm sector. Although the upper-level short-wave trough became deeper and the upper-level jet streak was divided into two regions at T = 24 h (Fig. 7d) and T = 36 h (Fig. 7f) during the CNTL run, the upper-level trough was shallower and the upper-level jet was straighter during the DRY run (Figs. 10d and f). Although the amplitude and pattern of the upper-level positive PV anomaly was almost same during the CNTL and DRY runs, the downstream negative PV anomaly disappeared only in the DRY run. More detailed structures can be seen in the trajectory analysis.

Air parcels, which moved upward in the middle level, disappeared in the DRY run (Fig. 13d) and the number of upward moving air parcels from the lower levels decreased, as compared with the CNTL run (Fig. 13c). Many air parcels rising near the cyclone center can be identified during the CNTL run (Fig. 14c) and the lower-level positive PV anomalies appeared over the surface cyclone center. Air parcels rapidly rose to a height of 7 km, moving eastward and the isentropic surface at 304 K was lifted up to the altitude where the upper-level negative PV anomaly located. However, during the DRY run, the lower-level positive PV anomaly disappeared, upward trajectories decreased, and the eastern tropopause was not lifted up. These differences are similar to the results in Davis et al. (1993), which suggested, using PV inversion analysis, that upward motion by latent heat release caused upward and northward advection of the tropopause aloft and enhanced the downstream upper-level ridge.

The CNTL and DRY runs of the PO-O cyclone exhibit the largest differences among the three cyclone types. First, surface cyclone development in the DRY run was much weaker than in the CNTL run. Although the deepening rate at T = 24 h and the minimum sea-level pressure were 2.26 Bergeron and 955 hPa, respectively, during the CNTL run (Table 1 and Fig. 2f), they were 0.71 Bergeron and 990 hPa during the DRY run, respectively. Vertically integrated rainwater spread over the warm sector as in the PO-L DRY run, and its amount and precipitable water remarkably decreased (Figs. 8 and 11). Although the northeastern upper-level jet streak appeared in the CNTL run, it did not appear in the DRY run. The upper positive and negative PV anomalies distinctly decreased in the DRY run.

Trajectory analysis also shows significant structural differences (Figs. 13e and f). During the CNTL run, air parcels with strong downdrafts (orange lines) intruded from the western upper levels of the cyclone and air parcels with strong updrafts (blue lines) suddenly rose up in the narrow area near the cyclone center from the western lower levels. The maximum updraft recorded speed was over 1.0 m s^{-1} at T = 24 h at 600 hPa in the CNTL run. In contrast, low-level air parcels with updrafts gradually rose up in the wide area during the DRY run (the updrafts had a maximum speed of 0.3 m s^{-1}). In addition, there were fewer air parcels with downdrafts (orange lines) during the DRY run. The differences of upward trajectories can be seen in vertical cross sections in Fig 14. In the CNTL run, the upward air parcels suddenly rose up just above the surface cyclone center where the lower-level positive PV anomalies appeared and reached up to 11 km in height (Fig 14e). The upward motion may have been forced by the upper-level positive PV anomaly because the anomaly was located just upstream of the surface cyclone.

The upwardly-moving air parcels, heated by latent heat release, were lifted up and diverged at the tropopause, creating the upper-level negative PV anomaly and the strong westerly jet along the northern side. In contrast to the PO-L DRY run, the positive PV anomaly as well as the upper-level negative PV anomaly weakened in the PO-O DRY run. The upward trajectories rose up to only 8 km and baroclinicity in whole troposphere weakened. The divergence did not occur at the upper levels and the northeastern upper-level jet streak did not appear at 300 hPa, as can be seen in Figs. 11 and 14f. These results reveal that the latent heat release near the cyclone not only created surface cyclonic circulation by positive PV anomaly formation, but also may have influenced the amplification of the upper-level trough and ridge through the upper negative PV anomaly formation. Although extremely rapid development was experience in the PO-O case, without latent heat release by the cyclone, interaction between the lower- and upper-level PV anomalies could not occur, and cyclogenesis was drastically slower and precipitation and water vapor convergence were reduced.

4. Discussion

The preceding analysis demonstrated the role of latent heat release in the three extreme cases, however an explanation of the reason for their "extremely" rapid development is still needed. To help to find the answer, three other cases were analyzed. These cyclones, referred hereafter to as standard cases, were selected based upon the similarity of their track and Eady index value to the extreme ones, previously discussed, but the maximum deepening rate was close to the regression line in Fig. 1 and larger than 1 Bergeron (triangles in Fig. 1). Figure 15 shows an upper-level PV anomaly that averaged between 200 and 500 hPa and vertically integrated rainwater at T = 24 h for the CNTL runs of the extreme and standard cases. At first, one can see that the approaching upper-level positive PV anomalies in the extreme cases were much stronger than in the standard cases. Although the amount of vertically integrated rainwater was larger in every extreme case, their patterns show similar tendencies among the types, i.e., the OJ cases were accompanied by smaller amounts of rainwater; the PO-L cases also had smaller amounts of rainwater extending eastward; and the PO-O cases had larger amounts and more systematic distribution of rain water near the cyclone center.

The meso-scale characteristic structures were also sensitive to latent heat release. Figures 16 and 17 show the results of the CNTL and DRY runs at T = 24 h for the standard cases. For the standard OJ runs, pressure, temperature and water vapor distributions in the lower level (Figs. 16a and b) and the positive PV anomaly in the upper level (Figs. 17a and b) were almost the same during the DRY and CNTL runs, with the exception of a smaller amount of vertically integrated rainwater and a somewhat weaker upper-level negative PV anomaly in the DRY run. For the standard PO-L runs, the amount of vertically integrated rainwater decreased, especially to the east of the cyclone center in the DRY run, and the pressure pattern became more rounded due to the absence of a depression from the latent heat release around the warm eastern frontal region (Figs. 16c and d). The influences of latent heat release appeared in the weaker upper-level negative PV anomaly, as was seen in the extreme PO-L cases (Figs. 17c and d). For the standard PO-O run, the influence of the latent heat release was the largest among the three standard runs, as had been seen in the extreme cases. Although vertically integrated rainwater amount maxima occurred near the surface cyclone center in the CNTL run, these rainwater maxima almost disappeared, water vapor concentration became weaker, and the cyclone center itself moved slightly northward during the DRY run (Figs. 16e and f). In the upper level, a strong negative PV anomaly and northwestern jet streak at the surface cyclone center disappeared and a positive PV anomaly moved northwestward in the DRY run (Figs. 17e and f). These lower-level and upper-level differences between the CNTL and DRY runs were consistent each cyclone case. Especially, the movement of the surface cyclone center revealed that latent heat release plays an important role in the cyclone development even in the standard case of the PO-O cyclone.

A series of comparisons between the extreme and standard cases suggest that although positive PV advection in the upper-level basically determined the extreme deepening, it is possible to say that meso-scale cyclonic features, in particular, the distribution and strength of the latent heat release (determined by the amounts of cloud and precipitation water), affect cyclone development through the nonlinear interaction among the upper-level short-wave trough, the jet (PV anomaly), and the latent heat release.

In the previous section, water vapor was determined to be an energy source for rapid cyclone development. However, after development, cyclones transport moisture for a considerable distance and affect the regional climate and/or the next-generation cyclone development (Lackmann et al. 1998, Smirnov and Moore 1999). To investigate moisture transport in the three extreme cases described in section 3, further analyses of backward air parcel trajectories and the water budget were conducted using the GANAL dataset, not simulated results, because of the long term integration of the simulation enhanced numerical errors, especially appearing in the determination of cyclone position and the precipitation distribution.

The size of the moisture budget was calculated by the amount of moisture in the air column and its local change. The size of the water vapor budget corresponds to the precipitation amount minus amount of the surface evaporation (P-E, where P is the amount of precipitation and E is the amount of surface evaporation), written as:

$$\mathrm{P}-\mathrm{E}=-\frac{\partial}{\partial t}\left(\frac{1}{g}\int_{p_t}^{p_b} q dp\right)-\frac{1}{g}\int_{p_t}^{p_b}\nabla\cdot(q\mathbf{v})dp, \tag{3}$$

where g is gravitational acceleration, q is specific humidity, p is pressure, p_t is the upper boundary of the air column (=300 hPa), p_b is sea-level pressure, $\mathbf{v}$ is the horizontal wind vector.

To calculate the trajectories of air parcels, vertical velocities were estimated using the kinematic method (O'Brien 1970). Backward trajectories start from the maximum point of vertically integrated vapor flux convergence, along the surrounding four grids at 500, 600, 700, 850, and 925 hPa levels, at the time of maximum deepening and 48 hours before and after its occurrence. Figure 19 shows backward trajectories of air parcels and precipitable water content averaged for 96 hours. Precipitation amounts, using 1 Degree Daily data (1DD) of the Global Precipitation Climatology Project (GPCP) (Huffman et al. 2001) accumulated during its lifecycle for the cyclone influence area, which is defined as the area within next SLP ridges, are plotted in the panel. Figure 19 shows similar composites of estimated P-E and vertical integrated water vapor flux using the GANAL dataset.

In the OJ case (Fig. 18a), the cyclone was located over the drier Asian continent at 48 hours before maximum deepening rate, and all air parcels came from the west during this time. There was no distinct precipitation around the cyclone center while the cyclone moved over the land. The precipitation amount maximized along the cold front over the northwestern Pacific Ocean during the occurrence of maximum deepening, as shown in Fig. 6. Air parcels in the lower level moved from the southward moisture area. For the backward trajectories 48 hours after the most rapid deepening, a maximum point of vertically integrated vapor flux convergence was located northeast of the Sea of Okhotsk. Air parcels in the lower level came from the Bering Sea and the central North Pacific Ocean, which is a relatively moist area. From the panels of P-E (Fig. 19a) and the GPCP precipitation amount (Fig. 18a), one can surmise that evaporation was greater over the Sea of Japan and south of Japan, and precipitation was larger over the Sea of Okhotsk and on both sides of the Kamchatka Peninsula. Stronger eastward vertically integrated vapor fluxes extended from the eastern coast of China to offshore of eastern Japan, where evaporation was dominant and northward fluxes appeared offshore of eastern Hokkaido, where precipitation was dominant. The results demonstrate that the warm sector of the OJ cyclone transported precipitation northward, while the cold sector absorbed heat and moisture from the ocean south of Japan, the Kuroshio current region.

In the PO-L case (Figs 18b and 19b), the cyclone tracked southward of the OJ case, and there was no distinct net moisture transport north of the cyclone track. After passing the Japanese islands, stronger precipitation occurred on the northern side, associated with the rapid deepening. The cyclone moved directly eastward and a larger amount of precipitation occurred around the track. Most of the air parcels came from the west and moved directly eastward, and a northward component of the vertically integrated vapor flux can be identified in the lower levels. The moisture budget and vapor flux analyses in Fig. 19b show that there were strong eastward vapor fluxes in the southern part of the cyclone track, which generated a large amount of precipitation over the eastern North Pacific and the west coast of the North American continent. A large amount of evaporation (P-E is about -45 mm day^{-1}) was identified in the western part of the North Pacific Ocean. Similar vapor fluxes and transportation were identified by Bao et al. (2006) using the Special Sensor Microwave Imager (SSM/I) dataset.

For the PO-O case, the cyclone formed along the east coast of China at 48 hours before maximum deepening. At that time, moist air parcels came from the vicinity of Taiwan, which is a very humid area (Fig. 18c), affecting the PO-O cyclone with moisture from the beginning. During the maximum deepening period, moist air parcels in the lower latitudes entered into the cyclone center, resulting in a large amount of precipitation, about 30 mm day^{-1}. 48 hours after the maximum deepening, the precipitation area moved to the western Bering Sea. During this period, moist air parcels came from the central North Pacific Ocean. Figure 19c shows that strong northward water vapor fluxes appeared within the eastern side of the cyclone track. A large amount of water vapor (P-E is -30 mm day^{-1}), evaporating over the ocean south of Japan was transported to the Kamchatka Peninsula and the central North Pacific.

In all three cases, a large amount of moisture evaporation occurred over the southern Japanese islands. These results are consistent with the results of a study conducted by Chen et al. (1995), which analyzed global water transports and suggested that the southern Japanese islands supplied a large amount of moisture to the atmosphere in winter. However, positive P-E and observed precipitation occurred in different areas during the three cyclones. Additionally, Yoshida and Asuma (2004) show that the direction and strength of the water vapor flux supplied to the cyclone center are different between the three types and the difference may affect the cyclone's rapid genesis. These results suggest that explosive cyclones may play an important role in global water circulation, especially during winter. A better understanding of the global water cycle requires an understanding of the variations in cyclone tracks and their mechanisms.

5. Summary and conclusions

The present study of explosive cyclogenesis in the northwestern Pacific region simulated six cyclone cases using PSU/NCAR MM5 and analyzed their evolutions. Extreme and standard cases of each cyclone type, i.e., OJ, PO-L, and PO-O, were examined. Cyclone types were classified by Yoshida and Asuma (2004) using cyclone tracks and most explosively developing positions. They followed characteristic evolutions, which could be successfully simulated using the meso-scale numerical model (PSU-NCAR MM5). Sensitivity experiments for latent heat release showed the importance of latent heat release in cyclogenesis, the differences among the three types and the similarities between explosive and standard cases in each type. The analysis of backward air parcel trajectories showed that the distribution of latent heat release was closely connected with cyclone structure and cyclogenesis.

Both OJ cases were not sensitive to latent heat release since the cyclone's precipitation area was far from the cyclone center, which resulted in weaker cyclogenesis than observed in the other types, caused mainly by the interaction between the upper vorticity advection and lower-level baroclinicity. The extreme PO-L case was somewhat sensitive to latent heat release, but the cyclone structure did not change much even during the DRY run because of a strong upper-level jet stream, the quick movement of the cyclone, and weaker precipitation. In contrast, the cyclone shape of the standard PO-L case varied under DRY runs because the contribution of latent heat release was relatively larger. The PO-O cases showed the most drastic responses to latent heat release. The deepening rate significantly decreased and the structures of the surface cyclone, as well as the upper-level jet stream, differed greatly between the control and sensitivity runs. These results may be attributed to the evolution and environment of the cyclones. The PO-O cyclones originally formed in the moist environment and developed with a large amount of precipitation. The environment of the PO-O cyclone formation may supply moist air easily into the lower level cyclone center. Thus, PO-O cyclones demonstrate more sensitivity to latent heat release than the other cases. In addition, the moisture budget and water vapor transport analyses showed that, although the moisture source area was almost the same region (the ocean south of Japan), the vapor transport direction and strength differed among the cyclone types resulting in precipitation in different areas.

In conclusion, the evolution of explosively developing cyclones is closely related to the cyclone meso-scale structure, reflecting the larger scale environment, in particular, the moisture supply and the upper PV anomaly, which leads to distribution of latent heat release. This suggests that detailed information concerning vapor distribution and winds over the ocean, and the positioning and depth of upper-level short-wave troughs is needed to improve the forecasting of explosively developing cyclones. Harr et al. (1992) reported that the cyclone track affected the success of forecasting, for which the evaluation of the role of diabatic heating in cyclogenesis was difficult. The results in the present paper are consistent with their results.

Additionally, a conceptual model of an extratropical cyclone, such as the Norwegian model or the Shapiro-Keyser model, may reflect the larger scale environments of the cyclones. The OJ cyclone has a tends to present with a distinct cold front and a stage to occlude structure, as shown in the Norwegian model, while the PO-O cyclone produces heavy precipitation around the warm front and cyclone center, leading to formation of bent-back warm front with a warm core, as shown in the Shapiro-Keyser model. Our cyclone classification may be able to contribute to a resolution of these problems. Fantini (2004) also reported that moisture affected the frontal structures using numerical simulations of the ideal cyclone.

The evolutions and structures of extratropical cyclones should be treated as interactions between the larger scale environment and smaller scale phenomena. Statistical analysis of the cyclones may be useful to understand these interactions. Observational research is also important. Recently, various satellites with microwave passive sensors and/or radar systems on-board have been used to monitor water bodies. Dropsondes, radar systems on aircraft, aerosondes and driftsondes are effective tools to observe the cyclone structure over the ocean. As most of the rapid deepening of cyclones occurs over the ocean, our observational knowledge is small, but should be increased for a better understanding of cyclones.

In contrast, the effects of explosively developing cyclones on climate and their relationships to the climate change are still not understood. One of reasons is that realistic explosively developing cyclones cannot be simulated in the climate numerical models due to insufficient model resolution (Walthorn and Smith 1998). Recently developed computer systems may be able to research the interaction of climate change and meso-scale phenomena (Ohfuchi et al. 2004, Tomita et al. 2005, Shen et al. 2006). Clarifying the interaction between cyclone activity and climate change is an exciting topic for future research.

Acknowledgments

A part of this paper represents the first author's Ph.D dissertation at Hokkaido University. The authors would like to express their thanks to Masaya Kato, Division of Earth and Planetary Sciences, Graduate School of Science, Hokkaido University, for his technical assistance in the analyses, especially providing tools to operate MM5 and analyze its output. They would also like to express their thanks to Yoshi-Yuki Hayashi, Division of Earth and Planetary Sciences, Graduate School of Science, Hokkaido University, and Koji Yamazaki, Graduate school of Environmental Earth Science, Hokkaido University, for their suggestions and encouragement. Part of the research was supported by a "Grant-in-Aid for Scientific Research [(A)-(1)-No. 13373003]" of Ministry of Education, Culture, Sport, Science and Technology of Japan (Monbu-Kagaku-sho). GPCP data were provided by Laboratory for Atmospheres, NASA Goddard Space Flight Center (http://precip.gsfc.nasa.gov/).

Appendix

A sensitivity experiment using numerical models always includes parameterization problems. In the current study, the cumulus parameterization may have an important contribution to the rapid cyclone deepening because precipitation formation is a key factor. To estimate sensitivity of cumulus parameterization, several comparisons were conducted using two experimental setups; one has an additional finer nested domain of a 5 km grid without cumulus parameterization in a 15 km grid domain within a 45 km grid outer domain, and another one is a 15 km grid domain without cumulus parameterization within a 45 km grid outer domain. Figure A1 shows an example of the results of the extreme PO-O case at T = 24 h. Cyclone development in both cases, with the 5 km grid and the 15 km grid without cumulus parameterization, was almost the same as that observed during the extreme PO-O CNTL run. These results indicate that the arguments presented in this paper do not depend heavily on cumulus parameterization.

References

Bao, J.-W., S. A. Michelson, P. J. Neiman, F. M. Ralph, and J. M. Wilczak, 2006: Interpretation of enhanced integrated water vapor bands associated with extratropical cyclones: Their formation and connection to tropical moisture. *Mon. Wea. Rev.*, **134**, 1063-1080.

Chen, S.-J., Y.-H. Kuo, P.-Z. Zhang, and Q.-F. Bai, 1992: Climatology of explosive cyclones off the east Asian coast. *Mon. Wea. Rev*., **120,** 3029-3035.

Chen, S.-J., and L. Dell'Osso, 1987: A numerical case study of east Asian coastal cyclogenesis. *Mon. Wea. Rev*., **115,** 1127-1139.

Chen, T.-C., J.-M. Chen, and J. Pfaendtner, 1995: Low-frequency variations in the atmospheric branch of the global hydrological cycle. *J. Climate*, **8**, 92-107.

Davis, C. A., M. T. Stoelinga, and Y.-H. Kuo, 1993: The integrated effect of condensation in numerical simulations of extratropical cyclogenesis. *Mon. Wea. Rev.*, **121**, 2309-2330.

Dudhia, J., 1989: Numerical study of convection observed during the winter monsoon experiment using a mesoscale two-dimensional model. *J. Atmos. Sci*., **46,** 3077-3107.

Fantini, M., 2004: Baroclinic instability of a zero-PVE jet: Enhanced effects of moisture on the life cycle of midlatitude cyclones. *J. Atmos. Sci.*, 61, 1296-1307.

Grell, G. A., 1993: Prognostic evaluation of assumptions used by cumulus parameterizations. *Mon. Wea. Rev*., **121,** 764-787.

Grell, G. A., J. Dudhia, and D. R. Stauffer, 1995: A description of the fifth-generation Penn

State/NCAR Mesoscale Model (MM5). NCAR Tech. Note NCAR/TN-398+STR, 122pp.

Gyakum, J. R., and R. E. Danielson, 2000: Analysis of meteorological precursors to ordinary and explosive cyclogenesis in western North Pacific. *Mon. Wea. Rev.*, **128**, 851-863.

Harr, P. A., R. L. Elsberry, T. F. Hogan, and W. M. Clune, 1992: Forecasts of North Pacific maritime cyclones with the Navy Operational Global Atmospheric Prediction System. *Wea. Forecasting*, **7**. 456-467.

Huffman, G. J., R. F. Adler, M. Morrissey, D. T. Bolvin, S. Curtis, R. Joyce, B. McGavock, and J. Susskind, 2001: Global precipitation at one-degree daily resolution from multi-satellite observations. *J. Hydrometeor.*, **2**, 36-50.

Keyser, D., and M. A. Shapiro, 1986: A review of the structure and dynamics of upper-level frontal zones. *Mon. Wea. Rev.*, **114**, 452-499.

Kuo, Y.-H., and S. Low-Nam, 1990: Prediction of nine explosive cyclones over the western Atlantic Ocean with a regional model. *Mon. Wea. Rev*., **118,** 3-25.

Kuo, Y.-H., M. A. Shapiro and E. G. Donall, 1991: The interaction between baroclinic and diabatic processes in a numerical simulation of rapidly intensifying extratropical marine cyclone. *Mon. Wea. Rev*., **119,** 368-384.

Lackmann, G. M., J. R. Gyakum, and R. Benoit, 1998: Moisture transport diagnosis of a wintertime precipitation event in the Mackenzie River Basin. *Mon. Wea. Rev.*, **126**, 668-691.

Lindzen, R. S., and B. Farrell, 1980: A simple approximate result for the maximum growth rate of baroclinic instabilities. *J. Atmos. Sci.*, **37**, 1648-1654.

Liou, C.-S., and R. L. Elsberry, 1987: Heat budgets of analyses and forecasts of an explosively deepening maritime cyclone. *Mon. Wea. Rev.*, **115**, 1809-1824.

Mclay, J. G., and J. E. Martin, 2002: Surface cyclolysis in the North Pacific Ocean. Part III: composite local energetics of troposphere-deep cyclone decay associated with rapid surface cyclolysis. Mon. Wea. Rev., 130, 2507-2529.

Mullen, S. L., and D. P. Baumhefner, 1988: Sensitivity of numerical simulations of explosive oceanic cyclogenesis to changes in physical parameterizations. *Mon. Wea. Rev.*, **116**, 2289-2329.

Nuss, W. A., and S. I. Kamikawa, 1990: Dynamics and boundary layer processes in two Asian cyclones. *Mon. Wea. Rev*., **118,** 755-771.

O'Brien, J. J., 1970: Alternative solutions to the classical vertical velocity problem. *J. Appl. Meteor.*, **9**, 197-203.

Ohfuchi, W., H. Nakamura, M. K. Yoshioka, T. Enomoto, K. Takaya, X. Peng, S. Yamane, T. Nishimura, Y. Kurihara, and K. Ninomiya, 2004: 10-km mesh meso-scale resolving simulations of the global atmosphere on the Earth Simulator: Preliminary outcomes of AFES (AGCM for the Earth Simulator). *J. Earth Simulator*, **1,** 8–34.

Reisner, J. R., J. Rasmussen, and R. T. Bruintjes, 1998: Explicit forecasting of supercooled liquid water in winter storm using the MM5 mesoscale model. *Quart. J. Roy. Meteor. Soc*.,

124B, 1071-1107.

Roebber, P. J., 1984: Statistical analysis and updated climatology of explosive cyclones. *Mon. Wea. Rev*., **112**, 1577-1589.

Sanders, F., and J. R. Gyakum, 1980: Synoptic-dynamic climatology of the “bomb”. *Mon. Wea. Rev*., **108,** 1589-1606.

Sanders. F., S. L. Mullen, and D. P. Baumhefner. 2000: Ensemble simulations of explosive cyclogenesis at ranges of 2-5 days. *Mon. Wea. Rev.*, **128**, 2920-2934.

Shapiro, M., and Coauthors, 1999: A planetary-scale to mesoscale perspective of the life cycles of extratropical cyclones: The bridge between theory and observations. *The Life Cycles of Extratropical Cyclones*, M. Shapiro and S. Gronas, Eds., Amer. Meteor. Soc., 139-186.

Shen, B.-W., R. Atlas, J.-D. Chern, O. Reale, S-.J. Lin, T. Lee, and J. Chang, 2006: The 0.125 degree finite-volume general circulation model on the NASA Columbia supercomputer: Preliminary simulations of mesoscale vortices. *Geophys. Res. Lett.*, **33**, L05801, doi:10.1029/2005GL024594.

Smirnov, V. V. and G. W. K. Moore, 1999: Spatial and temporal structure of atmospheric water vapor transport in the Mackenzie River Basin. *J. Climate*, **12**, 681-696.

Takano, I., 2002: Analysis of an intense winter extratropical cyclone that advanced along the south coast of Japan. *J. Meteor. Soc. Japan*, **80**, 669-695.

Tomita, H., H. Miura, S. Iga, T. Nasuno, and M. Satoh, 2005: A global cloud-resolving simulation: Preliminary results from an aqua planet experiment. *Geophys. Res. Lett.*, **32**, L08805, doi:10.1029/2005GL022459.

Yoshida, A., and Y. Asuma, 2004: Structures and environment of explosively developing extratropical cyclones in the northwestern Pacific region. *Mon. Wea. Rev*., **132,** 1121-1142.

Walthorn, K. D. and P. J. Smith, 1998: The dynamics of an explosively developing cyclone simulated by a general circulation model. *Mon. Wea. Rev.*, **126**, 2764–2781.

Ward, J.H., 1963: Hierarchical grouping to optimize an objective function. *Journal of the American Statistical Association*, **58**, 236 -244.

Figure caption list

Figure 1. Scatter diagrams between the Eady index (horizontal axis) estimated for 300 and 1000 hPa horizontal winds and potential temperatures averaged over an area within a 1000 km radius from the cyclone center when observing the maximum deepening rate and maximum deepening rate (vertical axis) for (a) OJ; (b) PO-L; and, (c) PO-O cyclones. Bold lines are regression lines corresponding to equations for the correlation coefficient (r) given in the upper left panels. Squares show the extreme cases and triangles show the standard cases.

Figure 2. Surface cyclone tracks (solid lines, crosses represent 6-hour interval positions, closed circles show the position at every 0000 UTC) in the left column and time series of central sea-level pressure in right column between the formation (triangle) and the disappearance (square) by GANAL data; (a) and (b) are for the extreme OJ, (c) and (d) for the extreme PO-L, and (e) and (f) for the extreme PO-O cases. Stars show the minimum sea level pressure. Arrows show the maximum deepening rate. Broken lines show the results of CNTL runs and dotted lines show results of DRY runs.

Figure 3. Synoptic weather chart for the extreme OJ case. In left column, sea level pressure (solid line, contour intervals are 4 hPa), potential temperature at 850 hPa (broken line, contour intervals are 2 K), and horizontal gradient of potential temperature at 850 hPa (shading). L shows the surface cyclone center. In the right column, the geopotential

height (solid line, contour intervals area 120 m), potential vorticity (broken line, contour intervals are 1 PVU = 10^{-6} m^{-2} s^{-1} K kg^{-1}) and wind speed (shading) at 300 hPa; (a) and (b) are at 1200 UTC 26 February 1999, (c) and (d) at 1200 UTC 27 February 1999, and (e) and (f) at 1200 UTC 28 February 1999.

Figure 4. Same as Fig. 3, but for extreme PO-L case; (a) and (b) are at 1800 UTC 9 February 1998, (c) and (d) at 1800 UTC 10 February 1998, and (e) and (f) at 1800 UTC 11 February 1998.

Figure 5. Same as Fig. 3, but for the extreme PO-O case; (a) and (b) are at 0000 UTC 30 December 1997, (c) and (d) at 0000 UTC 31 December 1997, and (e) and (f) at 0000 UTC 1 January 1998.

Figure 6. Sea level pressure (thin solid line, contour intervals are 4 hPa), potential temperature at 850 hPa (broken line, contour intervals are 4 K), vertically integrated rainwater (thick solid line, 0.2 and 2 mm are contoured), and precipitable water (shading) in left column. Geopotential height (solid line, contour intervals are 120 m), potential vorticity anomaly from 2 days average (shading), and horizontal wind speed (bold line, contour intervals are 10 m s^{-1} and plotted larger than 50 m s^{-1}) at 300 hPa in right column. (a) (b) T = 12 h, (c) (d) T = 24 h, (e) (f) T = 36 h of the extreme OJ CNTL run. L is the position of surface cyclone center and A-A' line is cross section in Fig. 14a.

Figure 7. Same as Fig. 6, but for the extreme PO-L CNTL run.

Figure 8. Same as Fig. 6, but for the extreme PO-O CNTL run.

Figure 9. Same as Fig. 6, but for the extreme OJ DRY run.

Figure 10. Same as Fig. 6, but for the extreme PO-L DRY run.

Figure 11. Same as Fig. 6, but for the extreme PO-O DRY.

Figure 12. Schematic illustration of the initial arrangement of air parcels for backward trajectory analysis. L represents the surface cyclone center at the maximum deepening rate.

Figure 13. Major trajectories for the extreme (a) OJ CNTL, (b) OJ DRY, (c) PO-L CNTL, (d) PO-L DRY, (e) PO-O CNTL and (f) PO-O DRY runs. Sea level pressure (solid line, contour intervals are 4 hPa) and precipitable water (shading) at T = 24 h are shown at the bottom.

Figure 14. Vertical cross section of projected trajectories rising near the surface cyclone center (thin line, corresponding to blue lines in Fig. 12), potential vorticity anomaly from 2 days average (shading), potential temperature (medium line, contour intervals are 8 K) and wind speed (bold line, contour intervals are 10 m s^{-1}, plotted larger than 50 m s^{-1}) at T = 24 h for the extreme (a) OJ CNTL along A-A' in Fig. 6, (b) OJ DRY along B-B' in Fig. 9, (c) PO-L CNTL along C-C' in Fig. 7, (d) PO-L DRY along D-D' in Fig. 10, (e) PO-O CNTL along E-E' in Fig. 8 and (e) PO-O DRY along F-F' in Fig. 11.

Figure 15. Upper potential vorticity anomaly averaged between 200 hPa and 500 hPa from 2

days average (shading) and vertically integrated rainwater (solid line, mm) at T = 24 h for (a) the extreme OJ CNTL, (b) the standard OJ CNTL, (c) the extreme PO-L CNTL, (d) the standard PO-L CNTL, (e) the extreme PO-O CNTL, and (f) the standard PO-O CNTL runs.

Figure 16. Sea level pressure (thin solid line, contour intervals are 4 hPa), potential temperature at 850 hPa (broken line, contour intervals are 4 K), vertically integrated rainwater (thick solid line, 0.2 and 2 mm are contoured), and precipitable water (shading) for (a) the standard OJ CNTL, (b) the standard OJ DRY, (c) the standard PO-L CNTL, (d) the standard PO-L DRY, (e) the standard PO-O CNTL and (f) the standard PO-O DRY runs at T = 24 h.

Figure 17. Geopotential height (solid line, contour intervals are 120 m), potential vorticity anomaly from 2 days average (shading), and horizontal wind speed (bold line, contour intervals are 10 m s^{-1} and plotted larger than 50 m s^{-1}) at 300 hPa for (a) the standard OJ CNTL, (b) the standard OJ DRY, (c) the standard PO-L CNTL, (d) the standard PO-L DRY, (e) the standard PO-O CNTL and (f) the standard PO-O DRY runs at T = 24 h.

Figure 18. 48 hours backward trajectories of air parcels from vertically integrated vapor flux convergence maximum point at 500, 600, 700, 850, and 925 hPa (circles, color shows altitude of air parcel (hPa)) at the maximum deepening, and 48 hours before and after. Precipitable water amount averaged over 96 hours (contour) and precipitation amount

from GPCP composited near cyclone during cyclone lifetime (shading). White line and open circles show cyclone track (star: maximum deepening, triangle: 48 hours before maximum deepening, and square: 48 hours after maximum deepening). (a) the extreme OJ, (b) the extreme PO-L, and (c) the extreme PO-O cases.

Figure 19. Vertically integrated vapor flux (arrows) and P-E (color shading) composited near cyclone during cyclone lifetime. Cyclone tracks are same as Fig. 18, (a) the extreme OJ, (b) the extreme PO-L, and (c) the extreme PO-O cases.

Figure A1. Sea level pressure (thin solid line, contour intervals are 4 hPa), potential temperature at 850 hPa (broken line, contour intervals are 4 K), vertically integrated rainwater (thick solid line, 0.2 and 2 mm are contoured), and precipitable water (shading) in upper panels. Geopotential height (solid line, contour intervals are 120 m), potential vorticity anomaly from 2 days average (shading), and horizontal wind speed (bold line, contour intervals are 10 m s^{-1} and plotted larger than 50 m s^{-1}) at 300 hPa in bottom panels. (a) (d) CNTL, (b) (e) 15 km grid without cumulus parameterization, (c) (f) 5 km grid without cumulus parameterization at T = 24 h. L is the position of surface cyclone center.

Table caption list

Table 1. Deepening rate (units of Bergeron) at T = 24 h and maximum deepening rate for GANAL analysis, CNTL run and DRY run.

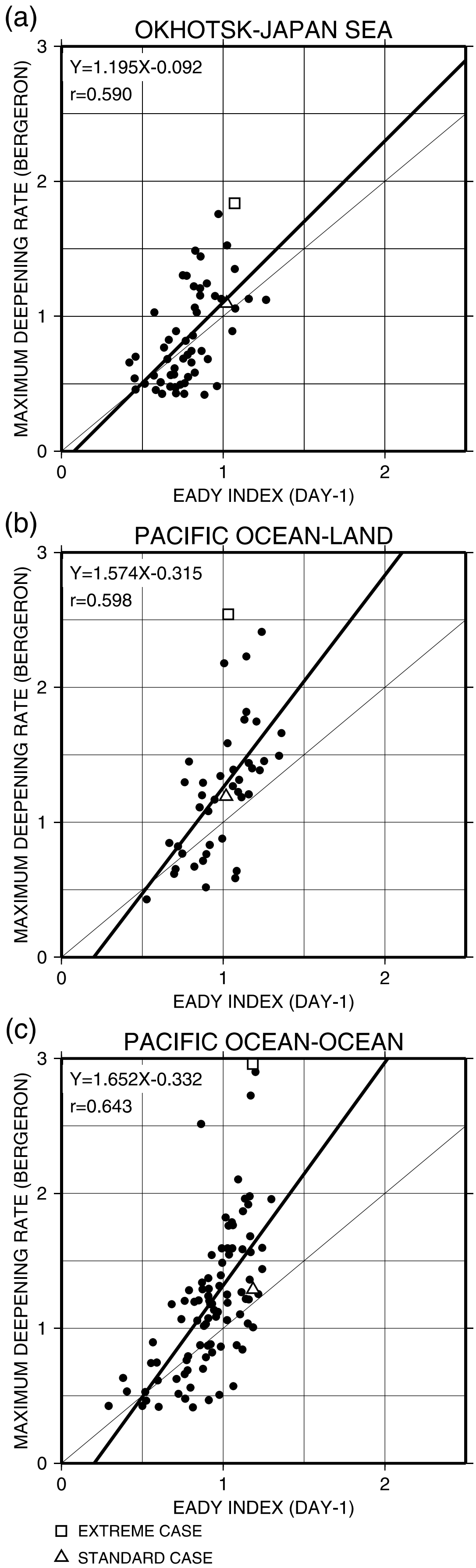

Figure 1. Scatter diagrams between the Eady index (horizontal axis) estimated for 300 and 1000 hPa horizontal winds and potential temperatures averaged over an area within a 1000 km radius from the cyclone center when observing the maximum deepening rate and maximum deepening rate (vertical axis) for (a) OJ; (b) PO-L; and, (c) PO-O cyclones. Bold lines are regression lines corresponding to equations for the correlation coefficient (r) given in the upper left panels. Squares show the extreme cases and triangles show the standard cases.

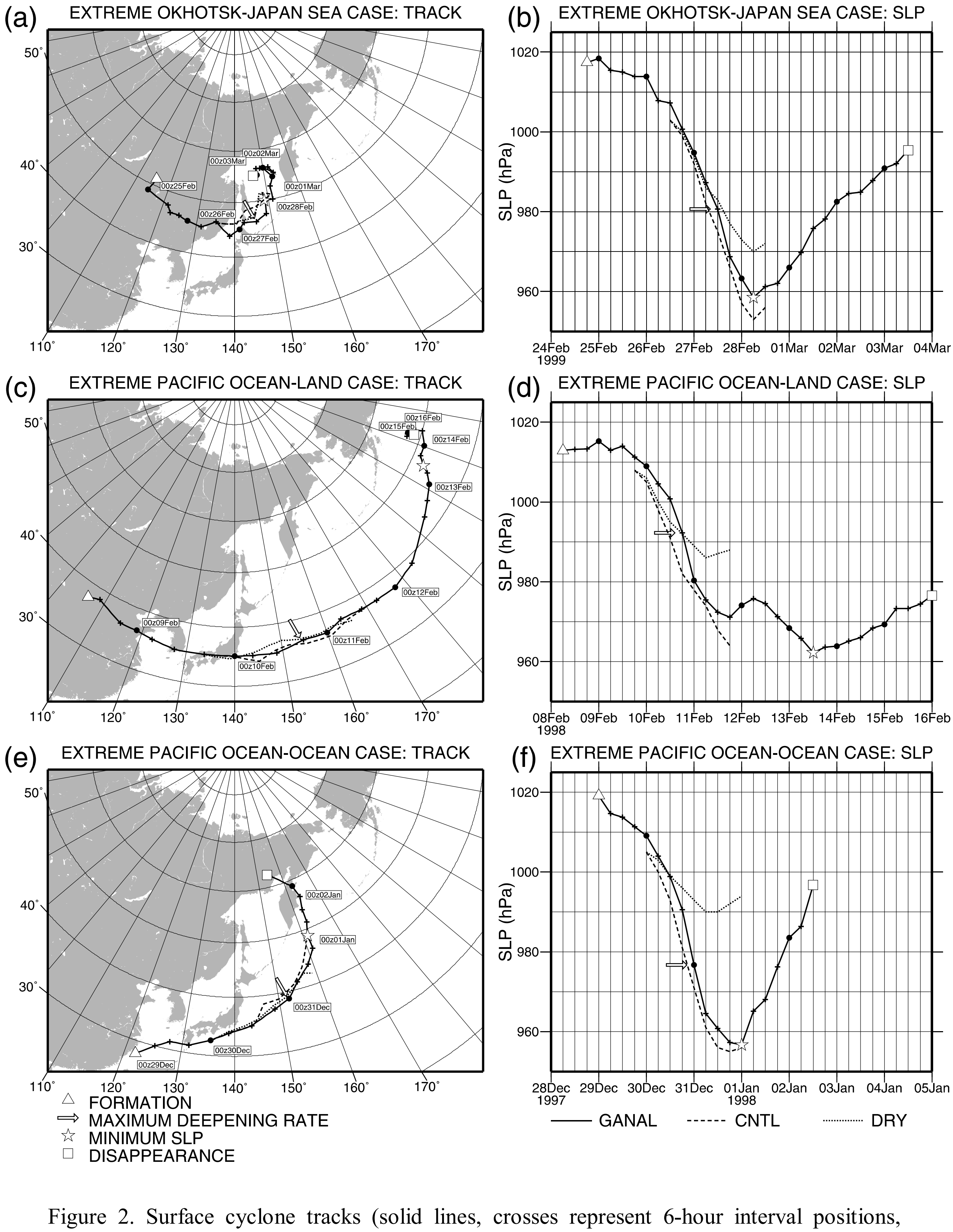

Figure 2. Surface cyclone tracks (solid lines, crosses represent 6-hour interval positions, closed circles show the position at every 0000 UTC) in the left column and time series of central sea-level pressure in right column between the formation (triangle) and the disappearance (square) by GANAL data; (a) and (b) are for the extreme OJ, (c) and (d) for the extreme PO-L, and (e) and (f) for the extreme PO-O cases. Stars show the minimum sea level pressure. Arrows show the maximum deepening rate. Broken lines show the results of CNTL runs and dotted lines show results of DRY runs.

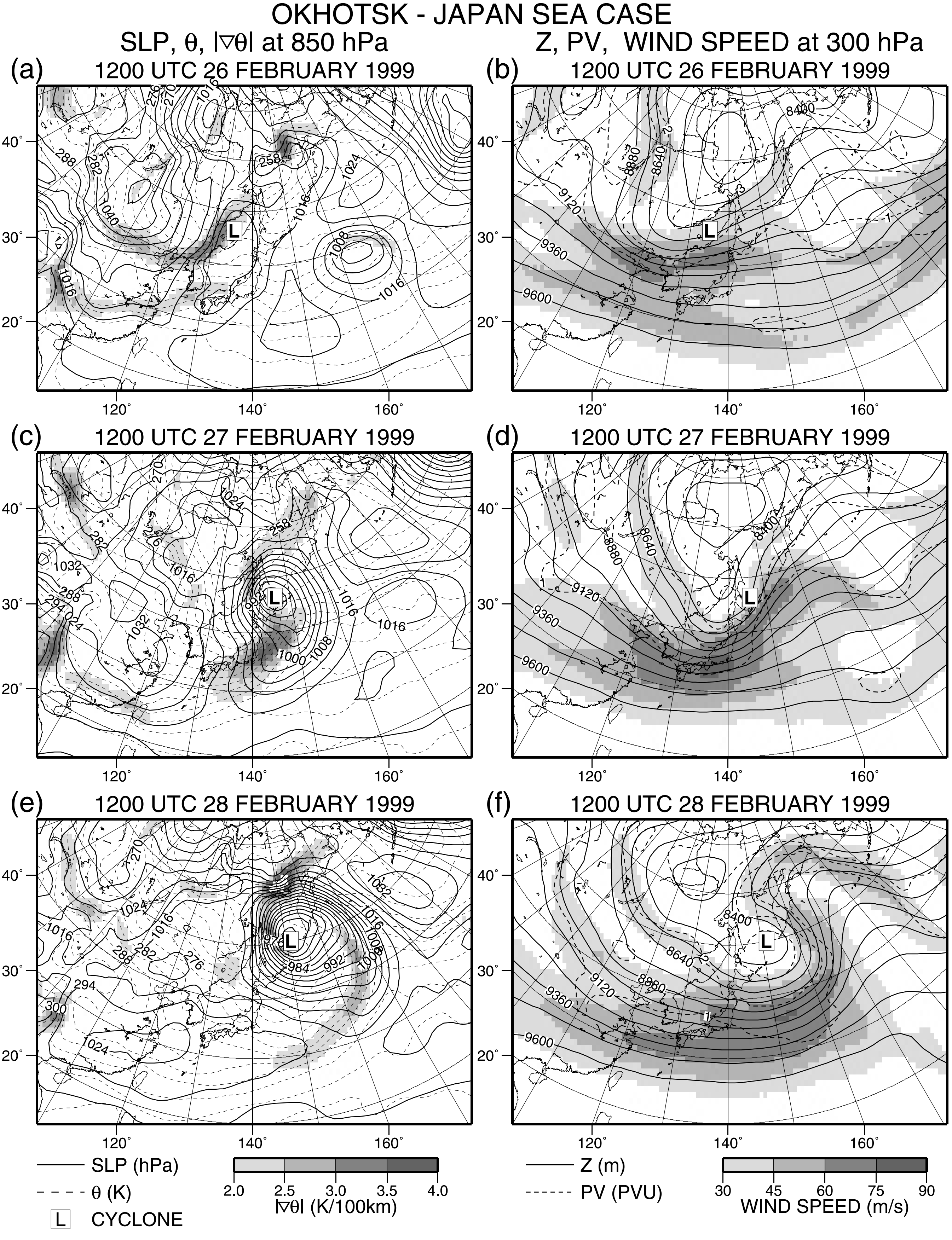

Figure 3. Synoptic weather chart for the extreme OJ case. In left column, sea level pressure (solid line, contour intervals are 4 hPa), potential temperature at 850 hPa (broken line, contour intervals are 2 K), and horizontal gradient of potential temperature at 850 hPa (shading). L shows the surface cyclone center. In the right column, the geopotential height (solid line, contour intervals area 120 m), potential vorticity (broken line, contour intervals are 1 PVU = 10^{-6} m^{-2} s^{-1} K kg^{-1}) and wind speed (shading) at 300 hPa; (a) and (b) are at 1200 UTC 26 February 1999, (c) and (d) at 1200 UTC 27 February 1999, and (e) and (f) at 1200 UTC 28 February 1999.

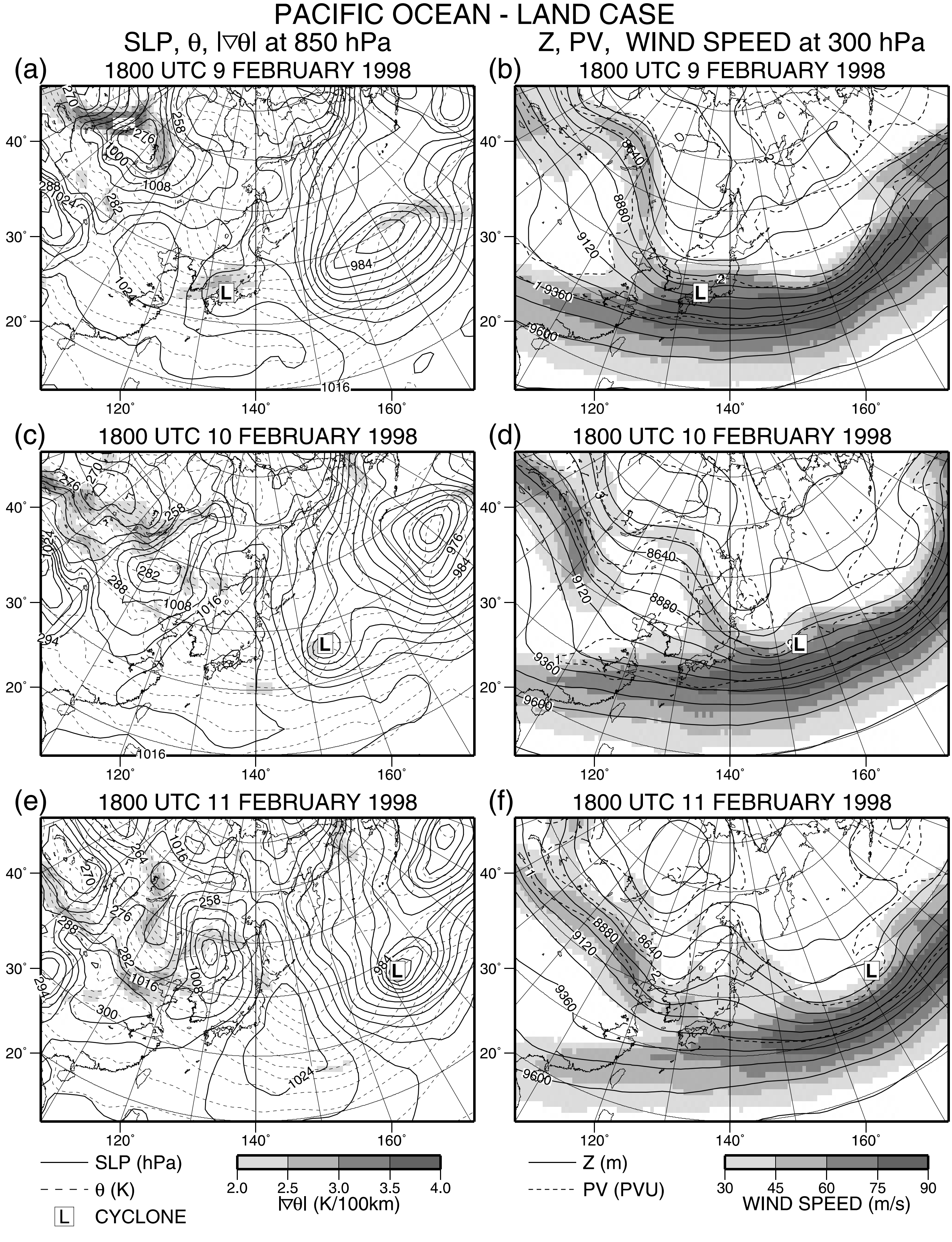

Figure 4. Same as Fig. 3, but for extreme PO-L case; (a) and (b) are at 1800 UTC 9 February 1998, (c) and (d) at 1800 UTC 10 February 1998, and (e) and (f) at 1800 UTC 11 February 1998.

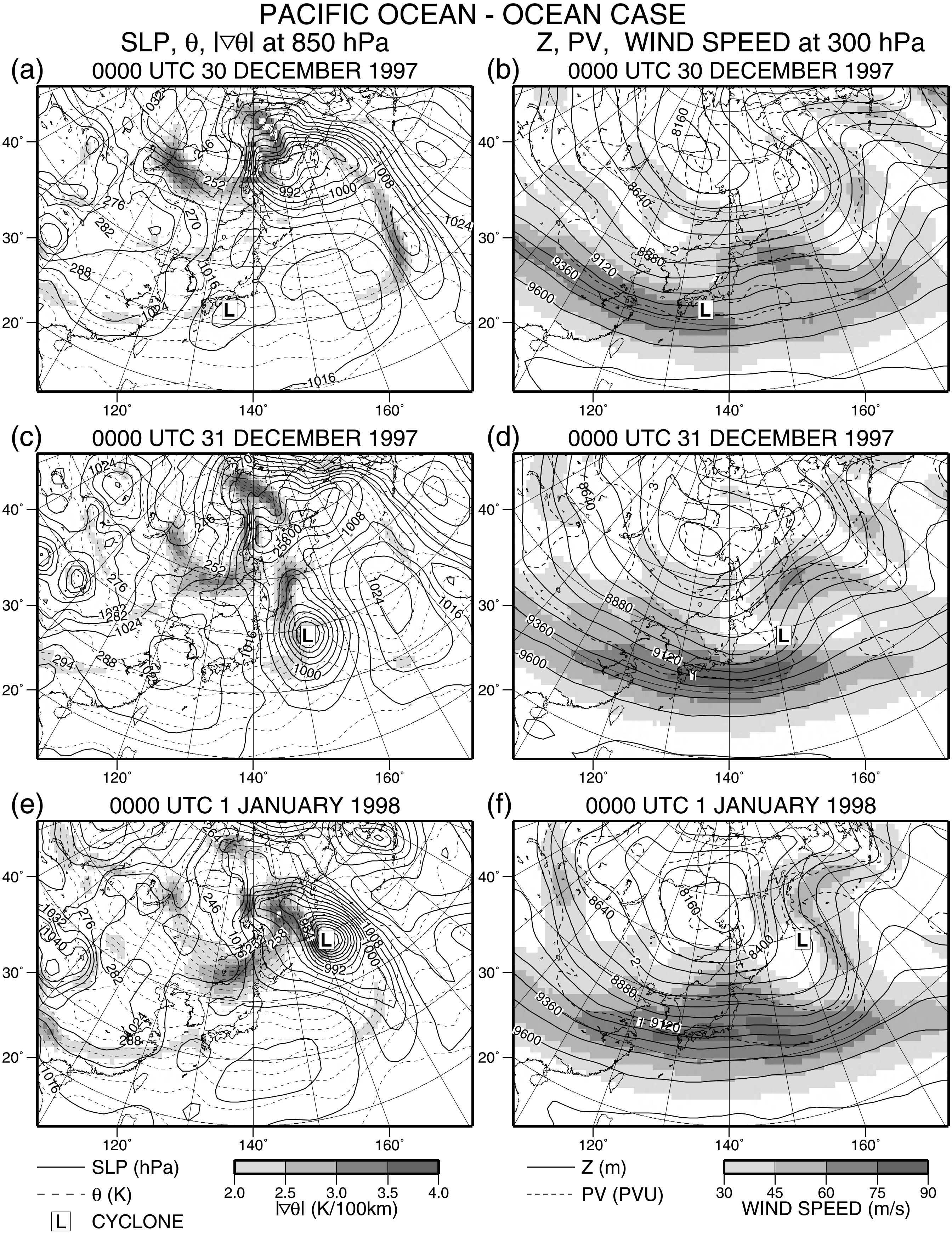

Figure 5. Same as Fig. 3, but for the extreme PO-O case; (a) and (b) are at 0000 UTC 30 December 1997, (c) and (d) at 0000 UTC 31 December 1997, and (e) and (f) at 0000 UTC 1 January 1998.

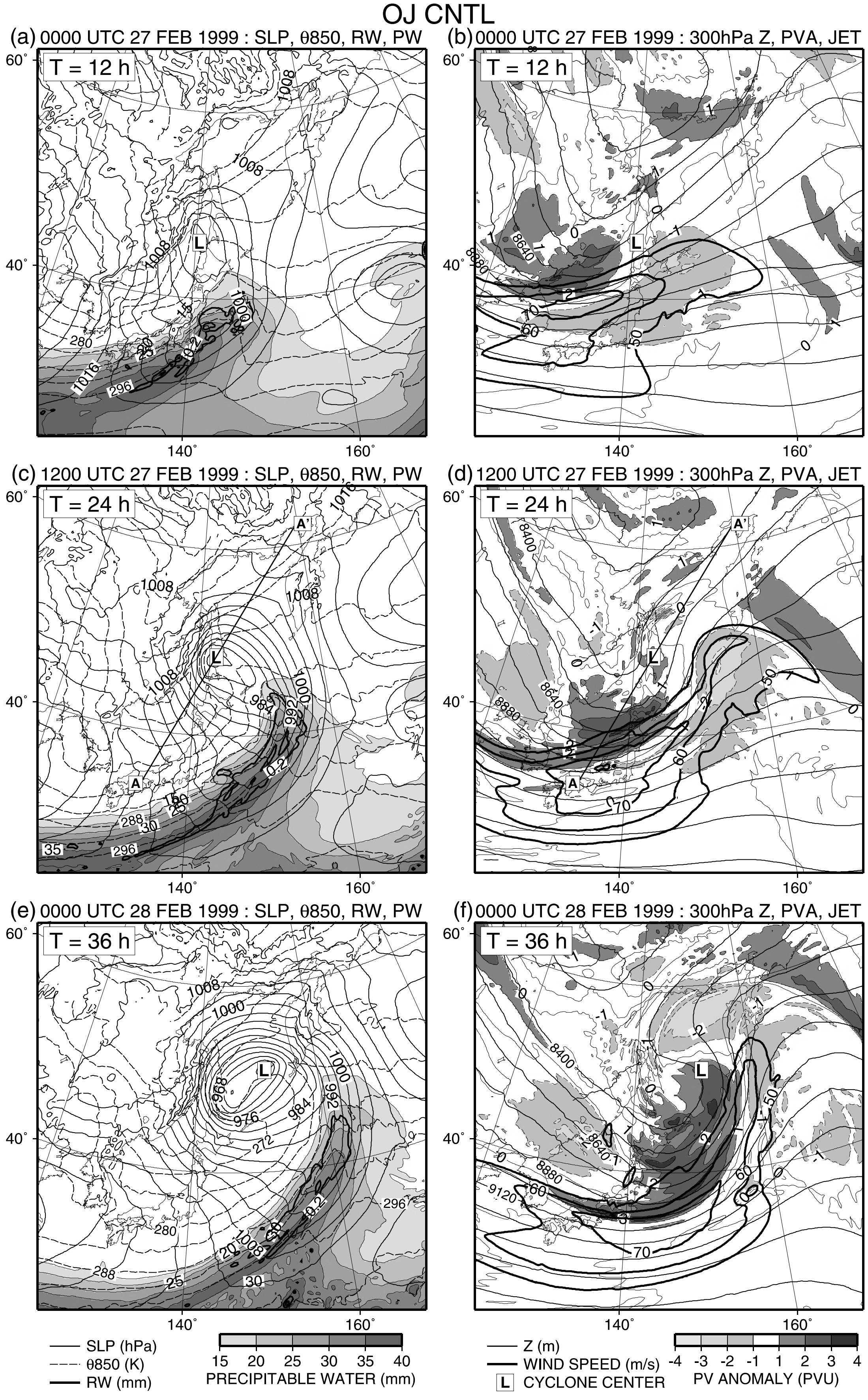

Figure 6. Sea level pressure (thin solid line, contour intervals are 4 hPa), potential temperature at 850 hPa (broken line, contour intervals are 4 K), vertically integrated rainwater (thick solid line, 0.2 and 2 mm are contoured), and precipitable water (shading) in left column. Geopotential height (solid line, contour intervals are 120 m), potential vorticity anomaly from 2 days average (shading), and horizontal wind speed (bold line, contour intervals are 10 m s^{-1} and plotted larger than 50 m s^{-1}) at 300 hPa in right column. (a) (b) T = 12 h, (c) (d) T = 24 h, (e) (f) T = 36 h of the extreme OJ CNTL run. L is the position of surface cyclone center and A-A' line is cross section in Fig. 14a.

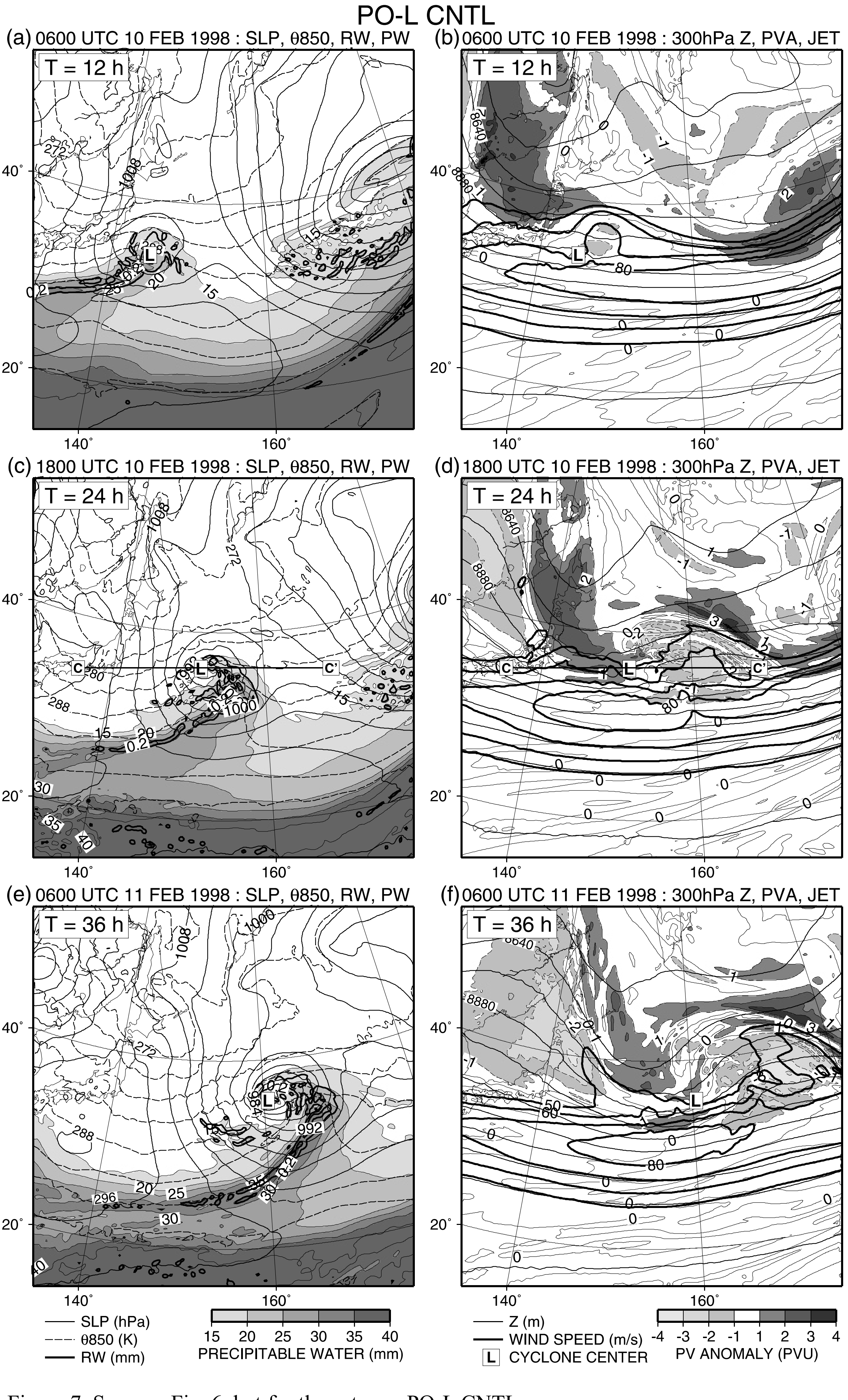

Figure 7. Same as Fig. 6, but for the extreme PO-L CNTL run.

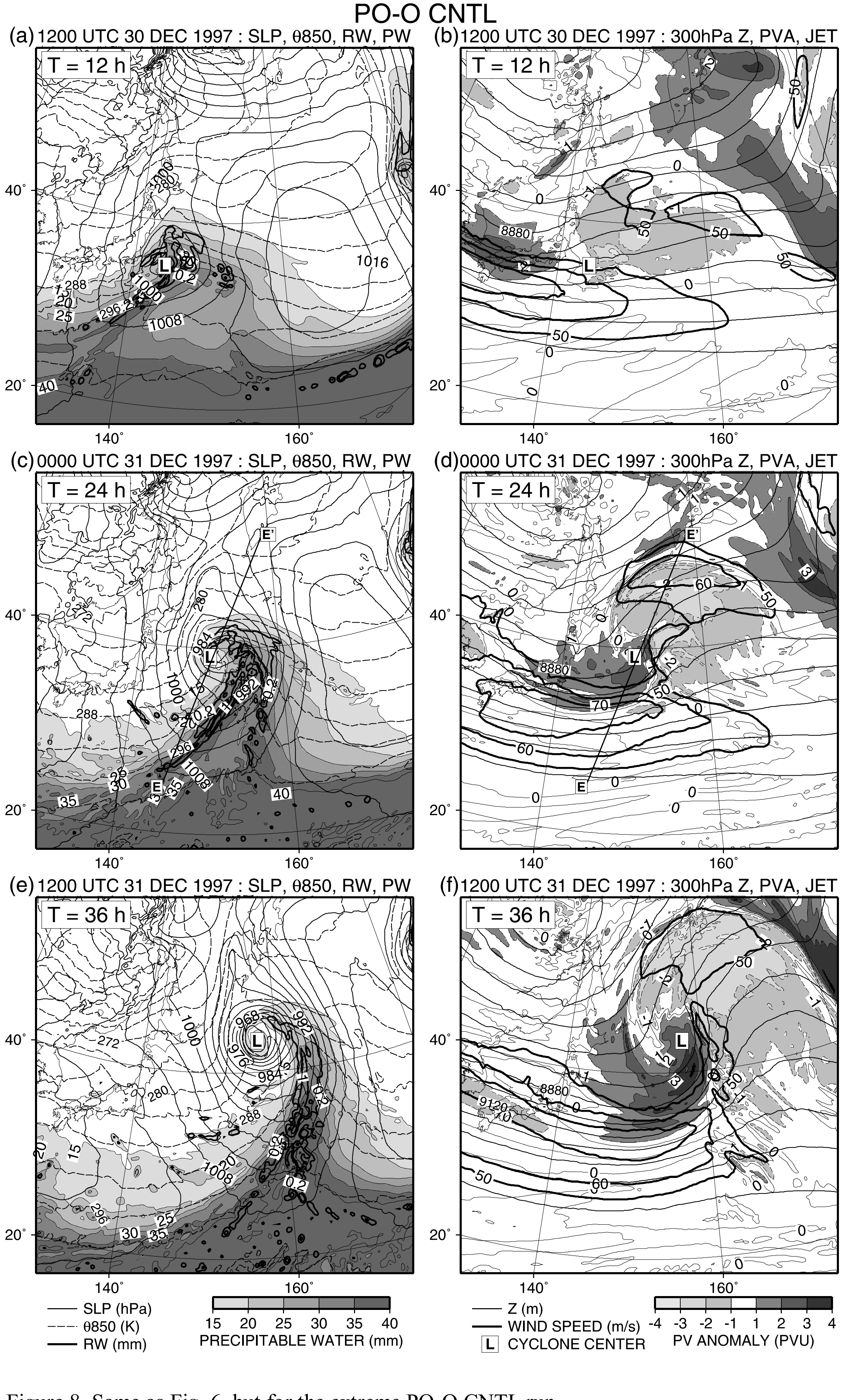

Figure 8. Same as Fig. 6, but for the extreme PO-O CNTL run.

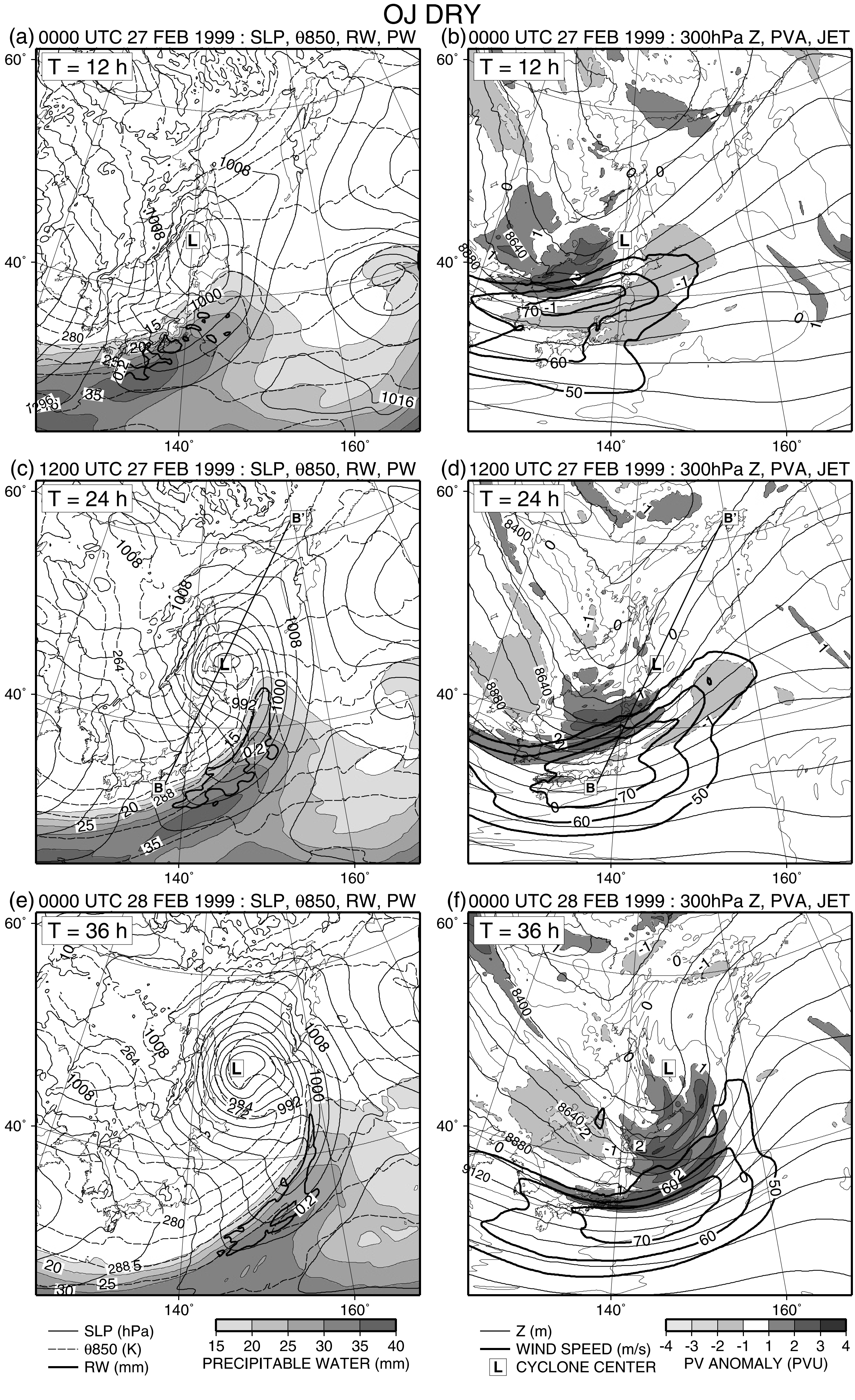

Figure 9. Same as Fig. 6, but for the extreme OJ DRY run.

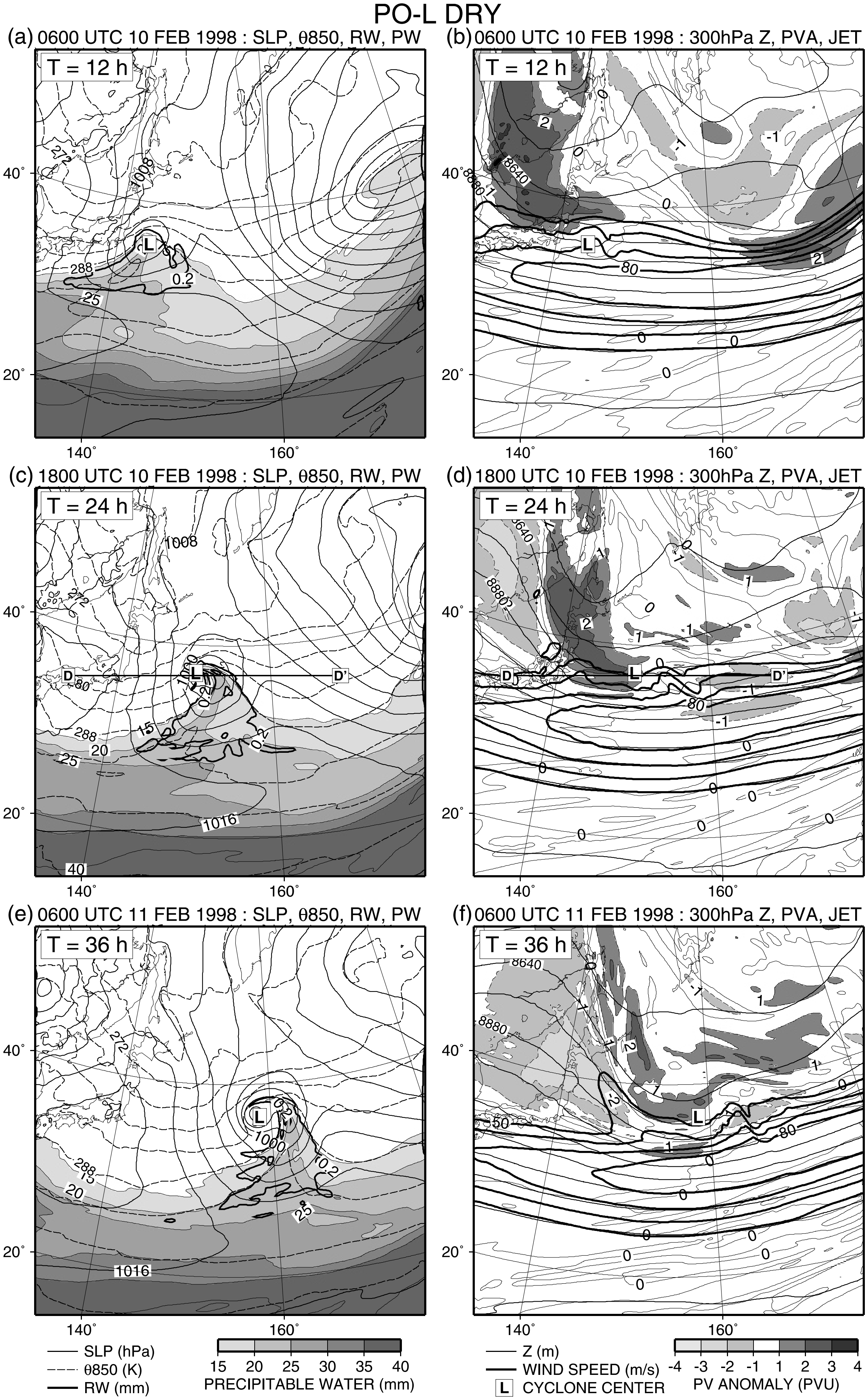

Figure 10. Same as Fig. 6, but for the extreme PO-L DRY run.

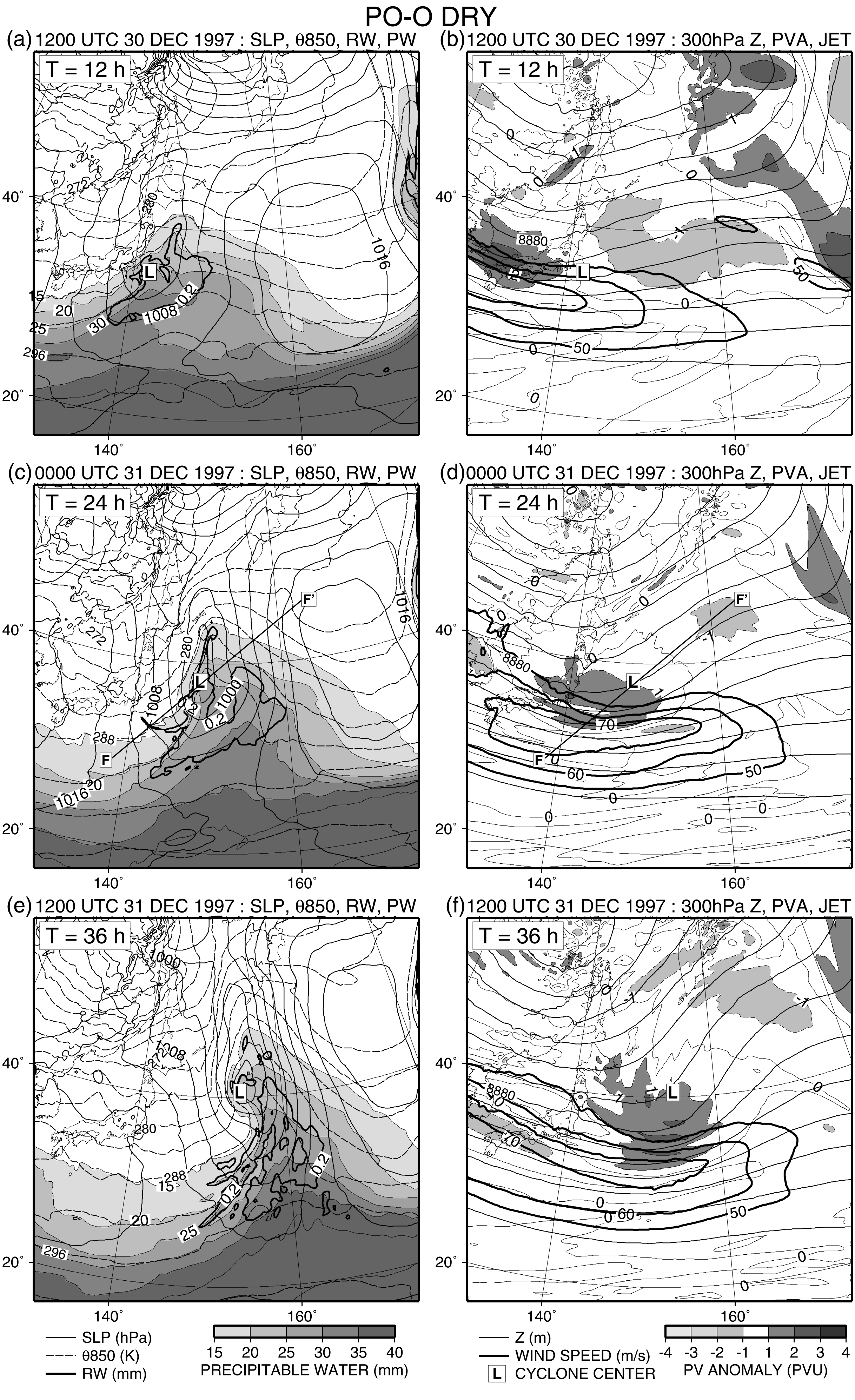

Figure 11. Same as Fig. 6, but for the extreme PO-O DRY.

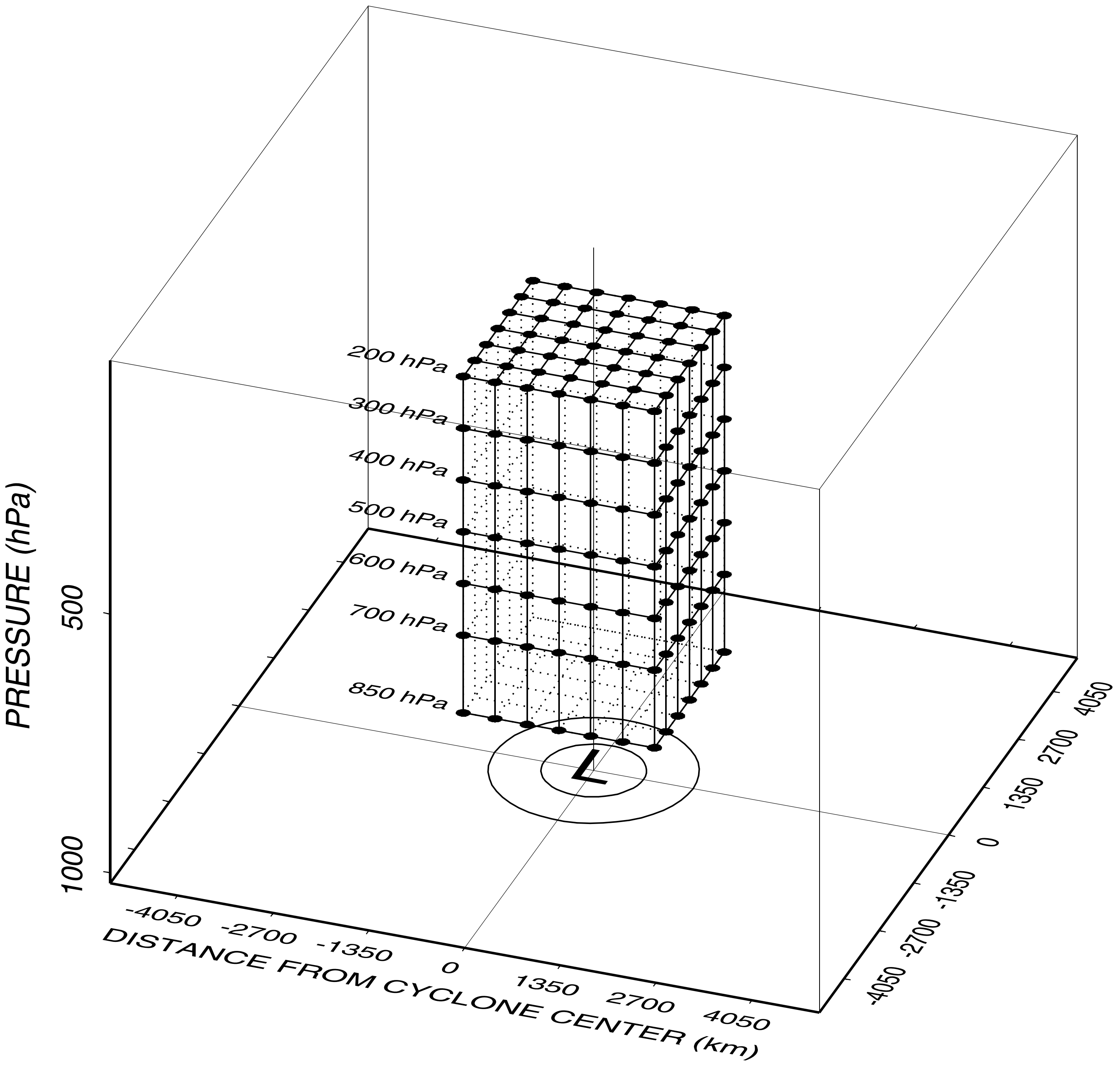

Figure 12. Schematic illustration of the initial arrangement of air parcels for backward trajectory analysis. L represents the surface cyclone center at the maximum deepening rate.

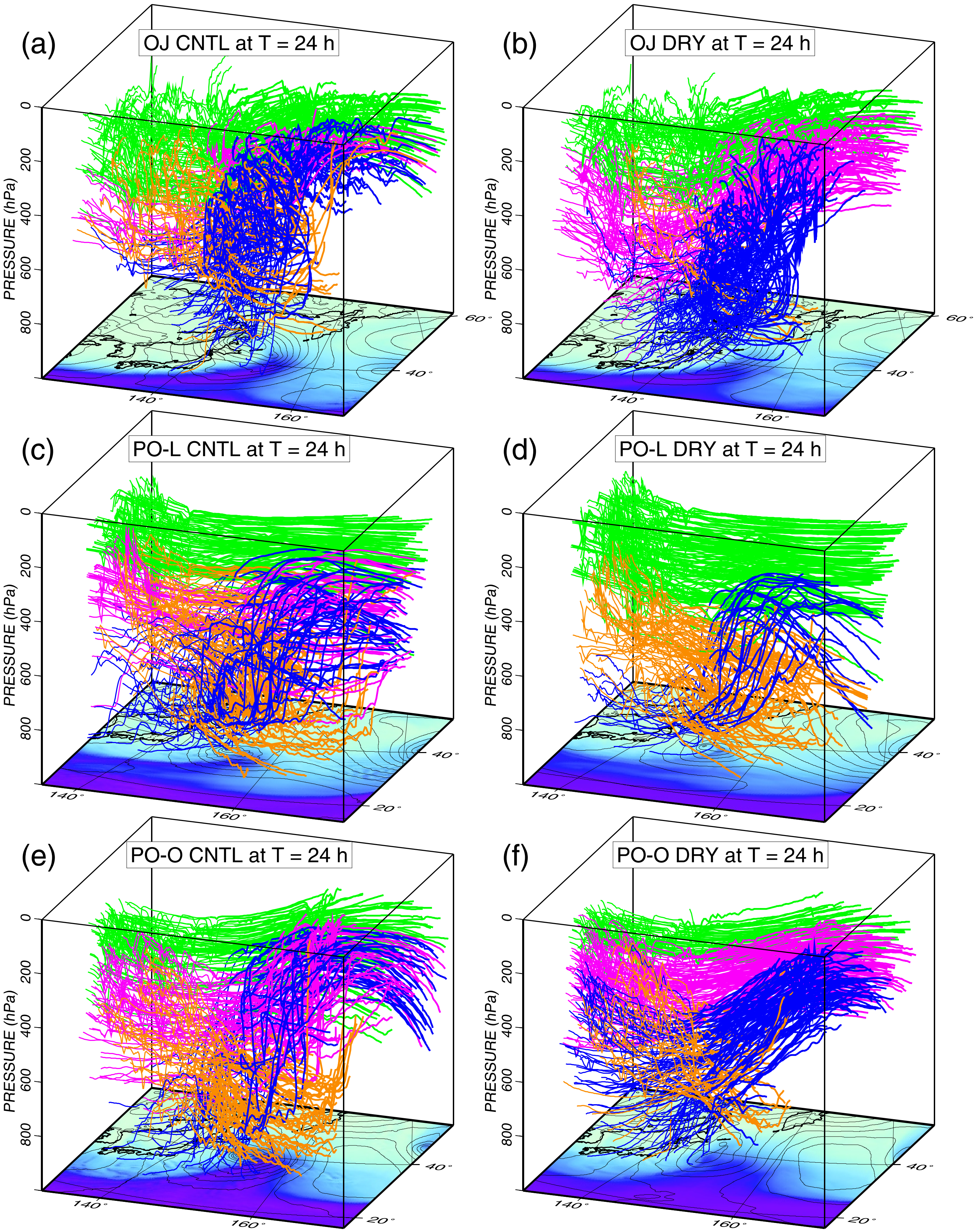

Figure 13. Major trajectories for the extreme (a) OJ CNTL, (b) OJ DRY, (c) PO-L CNTL, (d) PO-L DRY, (e) PO-O CNTL and (f) PO-O DRY runs. Sea level pressure (solid line, contour intervals are 4 hPa) and precipitable water (shading) at T = 24 h are shown at the bottom.

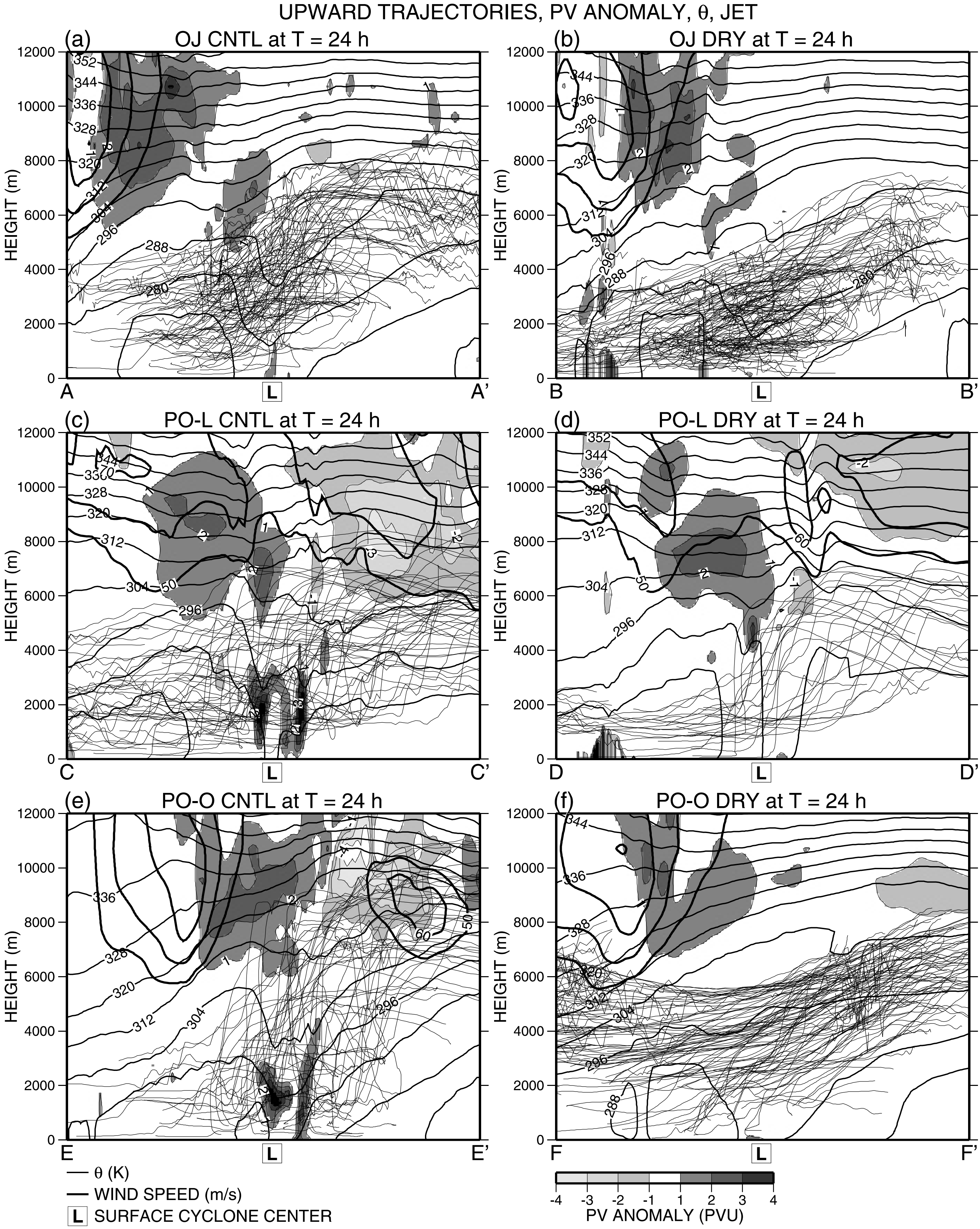

Figure 14. Vertical cross section of projected trajectories rising near the surface cyclone center (thin line, corresponding to blue lines in Fig. 12), potential vorticity anomaly from 2 days average (shading), potential temperature (medium line, contour intervals are 8 K) and wind speed (bold line, contour intervals are 10 m s^{-1}, plotted larger than 50 m s^{-1}) at T = 24 h for the extreme (a) OJ CNTL along A-A' in Fig. 6, (b) OJ DRY along B-B' in Fig. 9, (c) PO-L CNTL along C-C' in Fig. 7, (d) PO-L DRY along D-D' in Fig. 10, (e) PO-O CNTL along E-E' in Fig. 8 and (e) PO-O DRY along F-F' in Fig. 11.

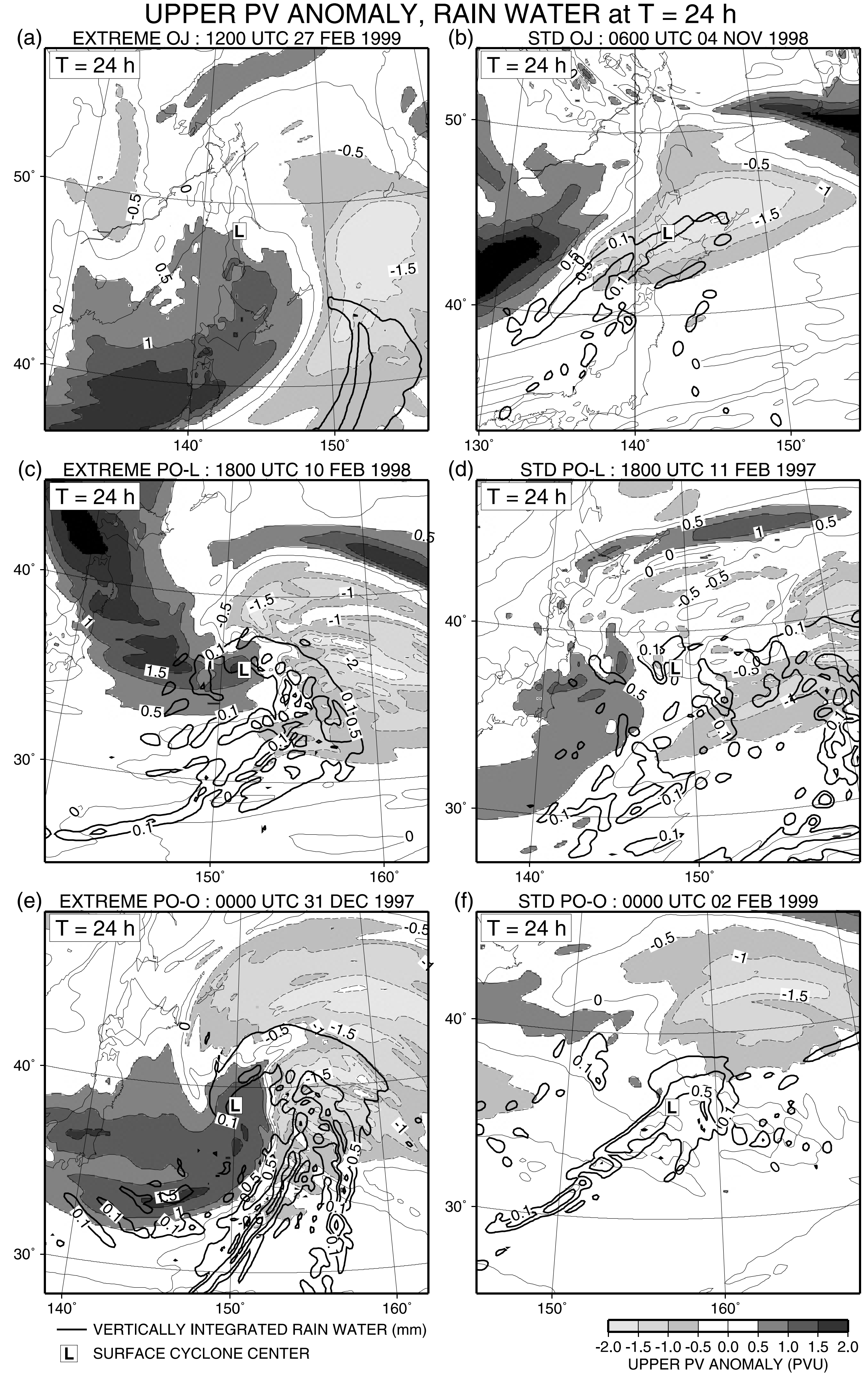

Figure 15. Upper potential vorticity anomaly averaged between 200 hPa and 500 hPa from 2 days average (shading) and vertically integrated rainwater (solid line, mm) at T = 24 h for (a) the extreme OJ CNTL, (b) the standard OJ CNTL, (c) the extreme PO-L CNTL, (d) the standard PO-L CNTL, (e) the extreme PO-O CNTL, and (f) the standard PO-O CNTL runs.

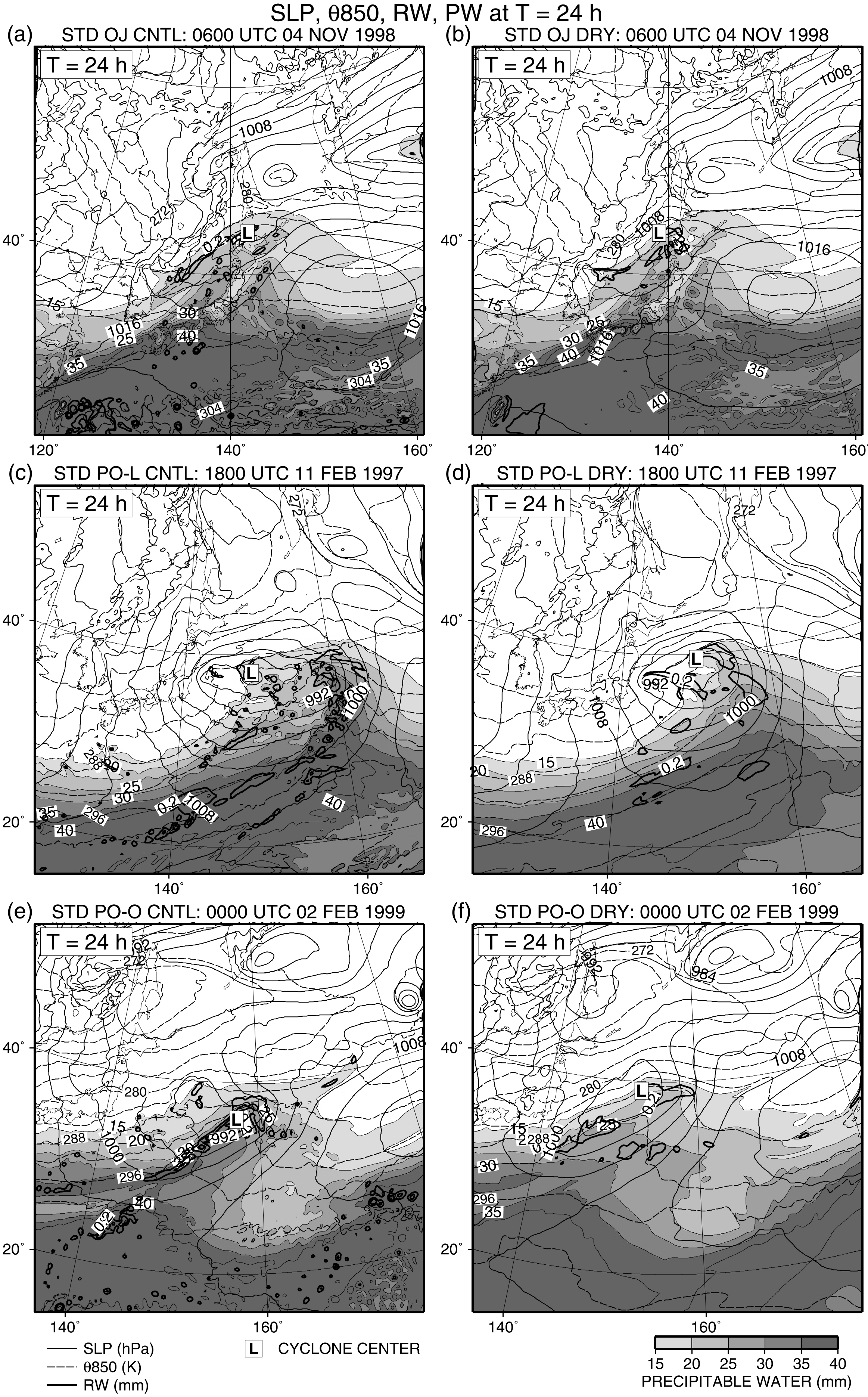

Figure 16. Sea level pressure (thin solid line, contour intervals are 4 hPa), potential temperature at 850 hPa (broken line, contour intervals are 4 K), vertically integrated rainwater (thick solid line, 0.2 and 2 mm are contoured), and precipitable water (shading) for (a) the standard OJ CNTL, (b) the standard OJ DRY, (c) the standard PO-L CNTL, (d) the standard PO-L DRY, (e) the standard PO-O CNTL and (f) the standard PO-O DRY runs at T = 24 h.

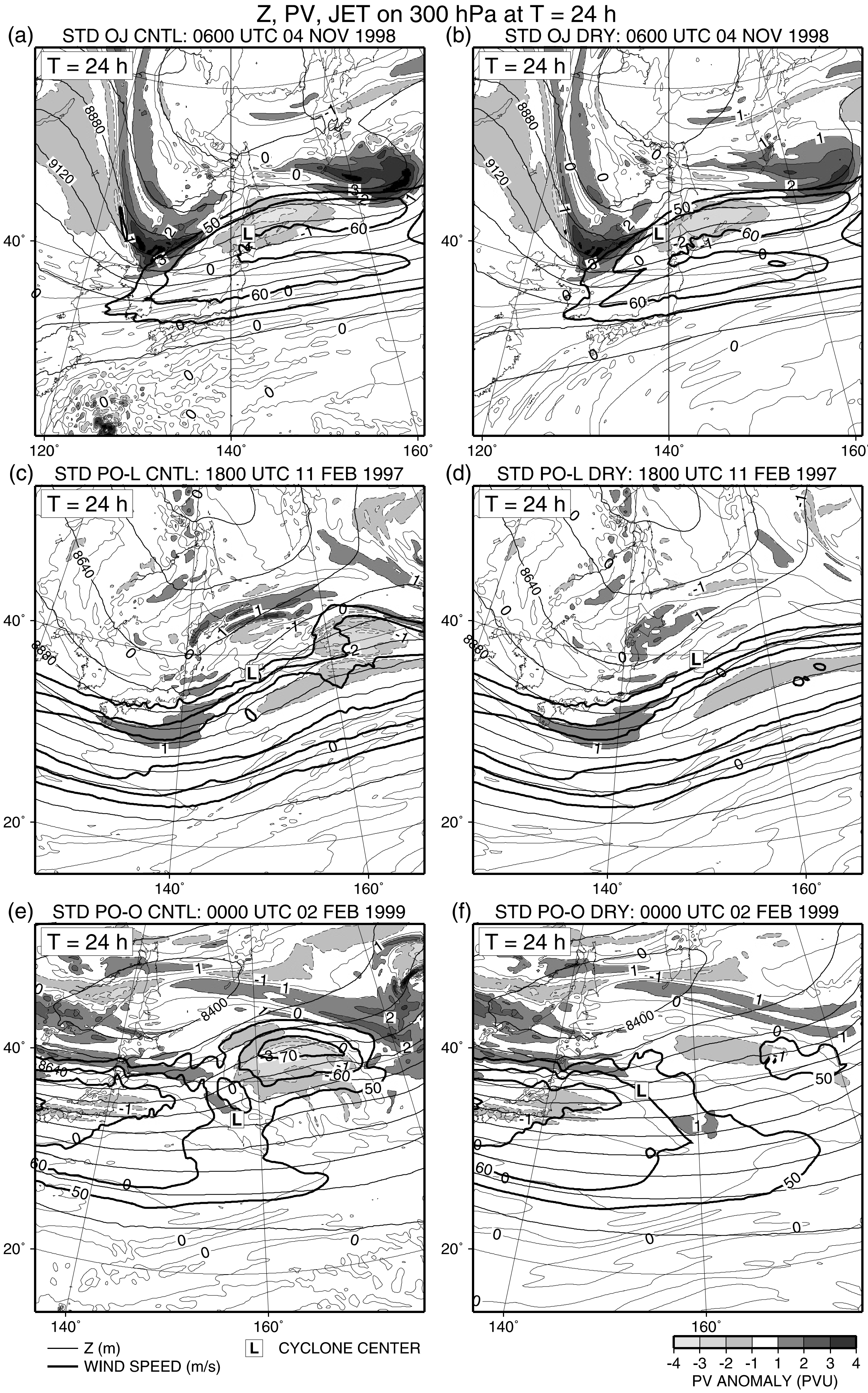

Figure 17. Geopotential height (solid line, contour intervals are 120 m), potential vorticity anomaly from 2 days average (shading), and horizontal wind speed (bold line, contour intervals are 10 m s^{-1} and plotted larger than 50 m s^{-1}) at 300 hPa for (a) the standard OJ CNTL, (b) the standard OJ DRY, (c) the standard PO-L CNTL, (d) the standard PO-L DRY, (e) the standard PO-O CNTL and (f) the standard PO-O DRY runs at T = 24 h.

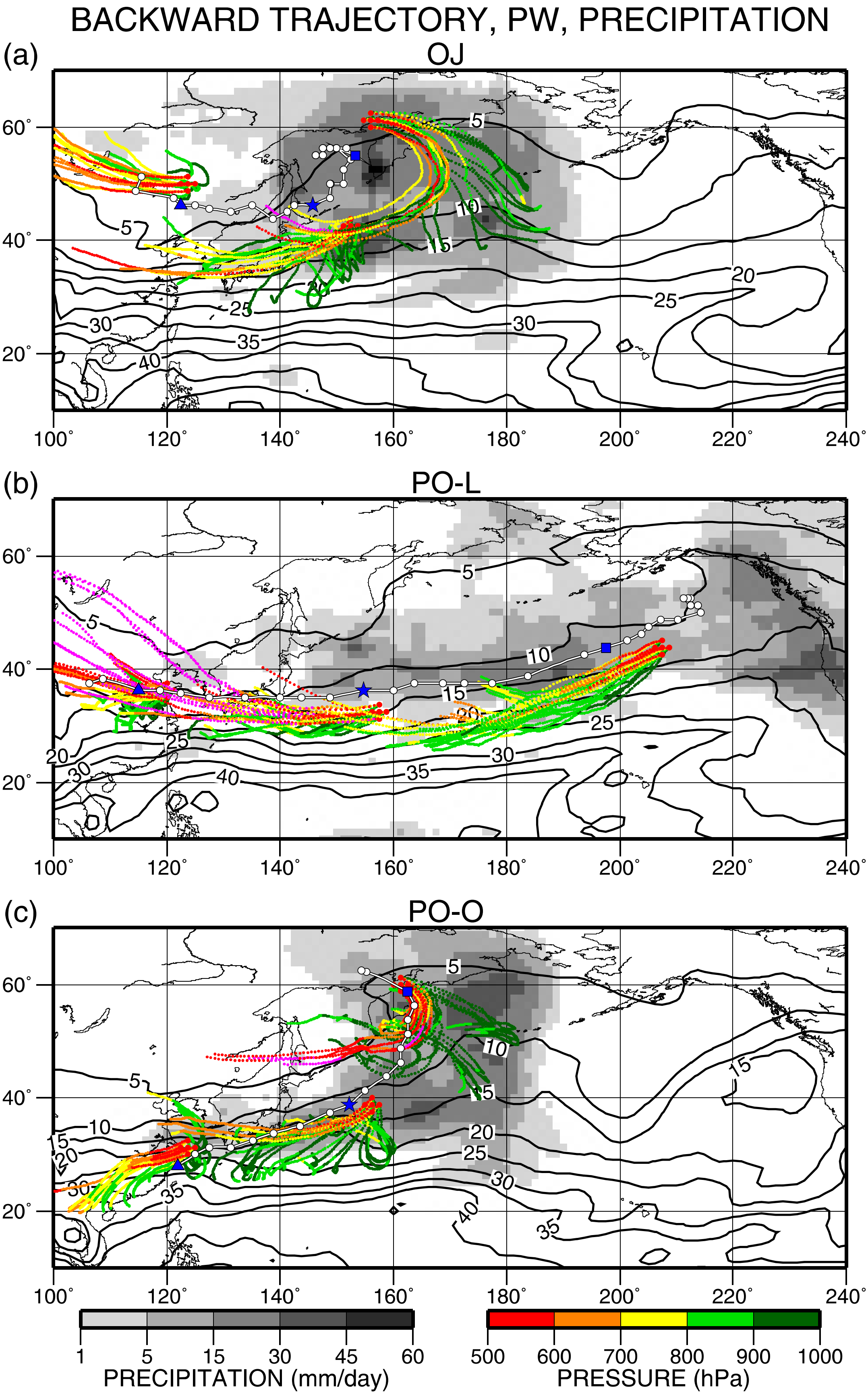

Figure 18. 48 hours backward trajectories of air parcels from vertically integrated vapor flux convergence maximum point at 500, 600, 700, 850, and 925 hPa (circles, color shows altitude of air parcel (hPa)) at the maximum deepening, and 48 hours before and after. Precipitable water amount averaged over 96 hours (contour) and precipitation amount from GPCP composited near cyclone during cyclone lifetime (shading). White line and open circles show cyclone track (star: maximum deepening, triangle: 48 hours before maximum deepening, and square: 48 hours after maximum deepening). (a) the extreme OJ, (b) the extreme PO-L, and (c) the extreme PO-O cases.

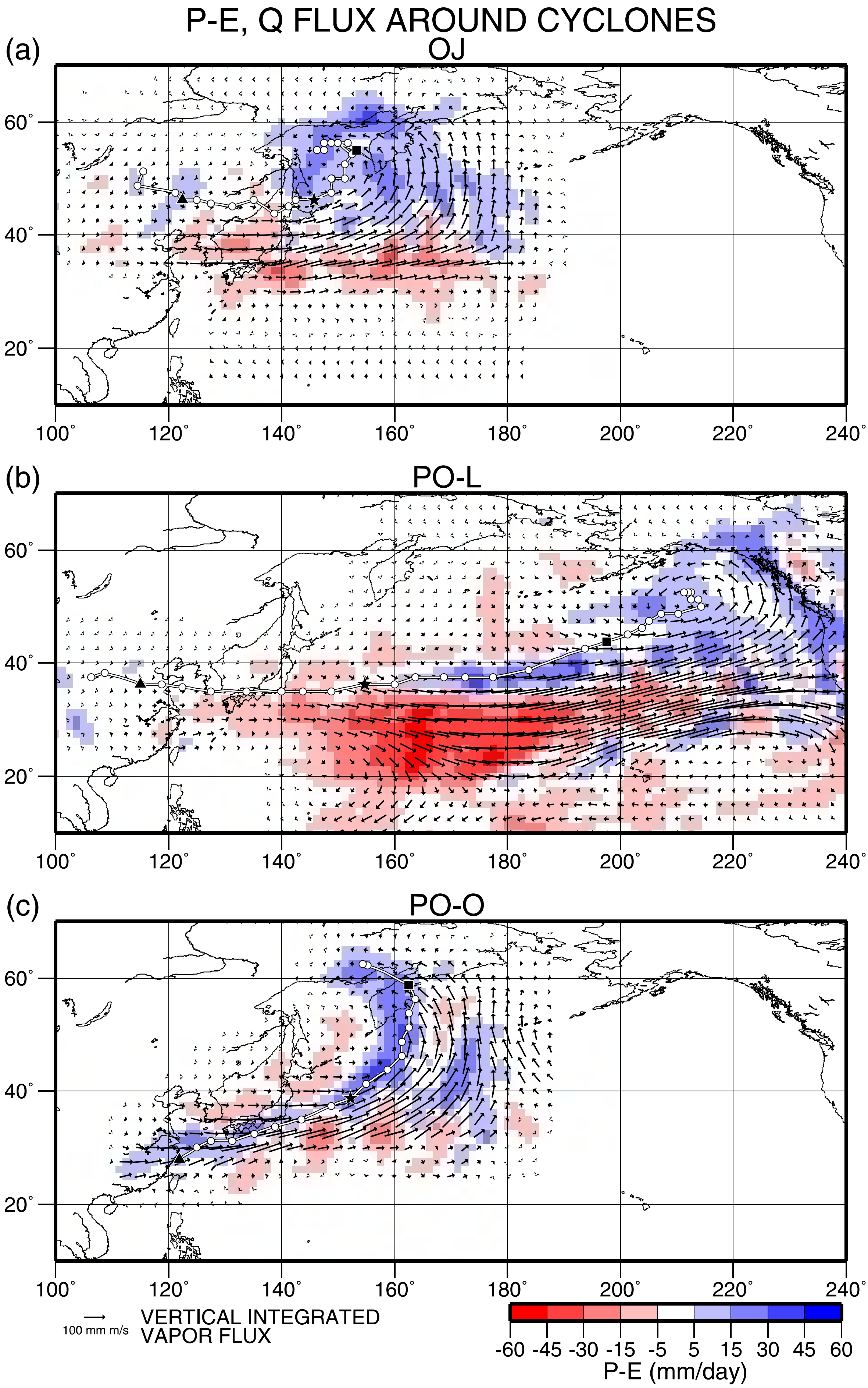

Figure 19. Vertically integrated vapor flux (arrows) and P-E (color shading) composited near cyclone during cyclone lifetime. Cyclone tracks are same as Fig. 18, (a) the extreme OJ, (b) the extreme PO-L, and (c) the extreme PO-O cases.

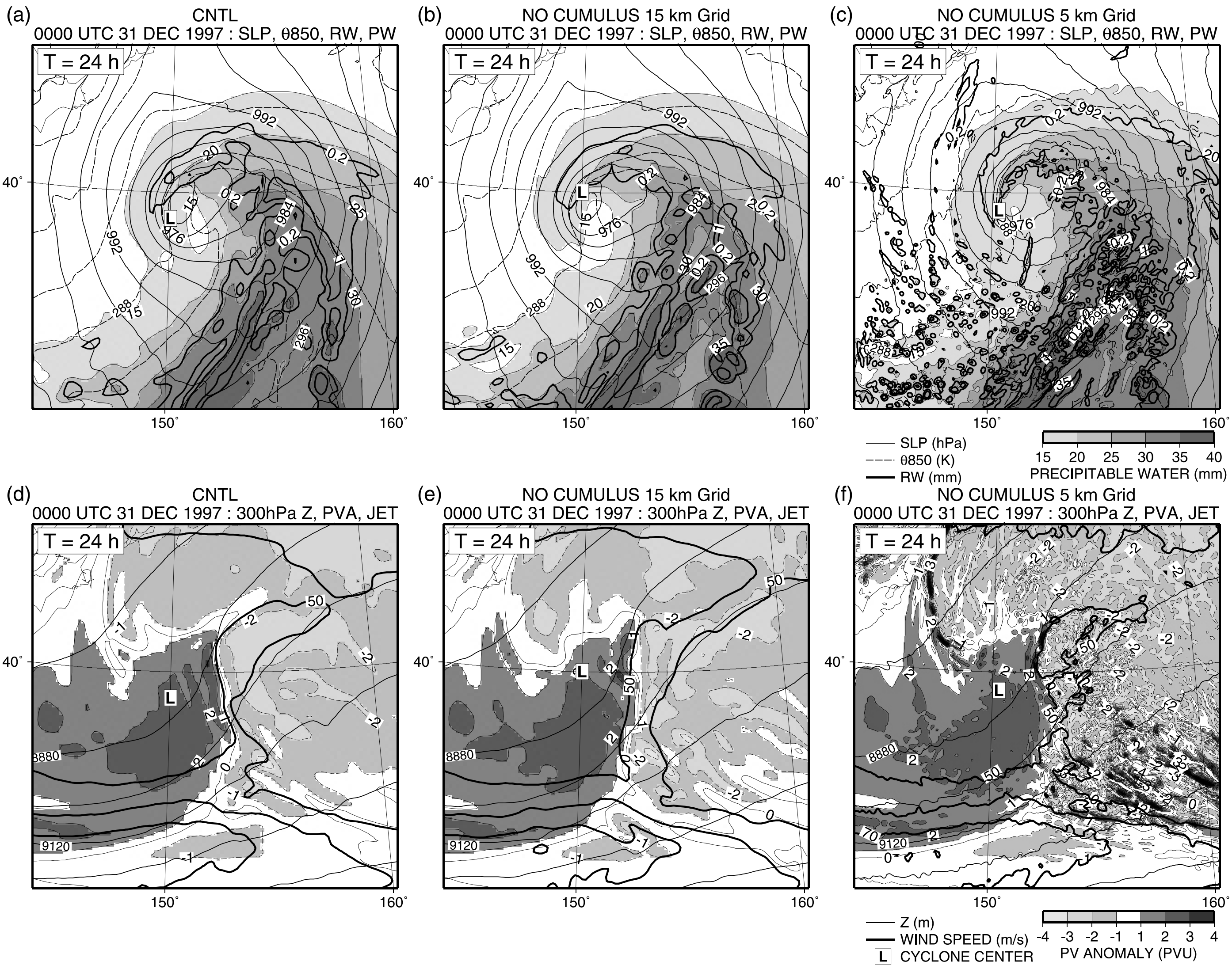

Figure A1. Sea level pressure (thin solid line, contour intervals are 4 hPa), potential temperature at 850 hPa (broken line, contour intervals are 4 K), vertically integrated rainwater (thick solid line, 0.2 and 2 mm are contoured), and precipitable water (shading) in upper panels. Geopotential height (solid line, contour intervals are 120 m), potential vorticity anomaly from 2 days average (shading), and horizontal wind speed (bold line, contour intervals are 10 m s^{-1} and plotted larger than 50 m s^{-1}) at 300 hPa in bottom panels. (a) (d) CNTL, (b) (e) 15 km grid without cumulus parameterization, (c) (f) 5 km grid without cumulus parameterization at T = 24 h. L is the position of surface cyclone center.

Table 1. Deepening rate (units of Bergeron) at T = 24 h and maximum deepening rate for GANAL analysis, CNTL run and DRY run.

Type	Deepening rate at T = 24 h (Maximum deepening rate, time)		
	GANAL	CNTL	DRY
OJ	1.84	1.55 (1.70, T=30h)	0.88 (1.40, T=12h)
PO-L	2.54	1.62 (2.01, T=18h)	0.73 (1.37, T=12h)
PO-O	2.96	2.26 (2.64, T=18h)	0.71 (0.88, T=12h)